Variability of Zooplankton and Sea Surface Temperature in the Southern Ocean

by

Ariane Verdy

B.Eng. Ecole Polytechnique de Montréal, 2001

Submitted in partial fulfillment of the requirements for the degree of

Master of Science

at the

MASSACHUSETTS INSTITUTE OF TECHNOLOGY

and the

WOODS HOLE OCEANOGRAPHIC INSTITUTION

February 2006

Author .....

Joint Program in Physical Oceanography
Massachusetts Institute of Technology
and Woods Hole Oceanographic Institution
February 2006

Certified by .....

Glenn R. Flierl
Professor of Oceanography
Thesis Supervisor

Accepted by .....

Joseph Pedlosky
Chair, Joint Committee for Physical Oceanography
Massachusetts Institute of Technology
and Woods Hole Oceanographic Institution

Variability of Zooplankton and Sea Surface Temperature in the Southern Ocean

by

Ariane Verdy

Submitted to the Joint Program in Oceanography at the Massachusetts Institute of Technology and the Woods Hole Oceanographic Institution, in partial fulfillment of the requirements for the degree of Master of Science

Abstract

Interactions between physical and biological processes in the Southern Ocean have significant impacts on local ecosystems as well as on global climate. In this thesis, I present evidence that the Southern Ocean circulation affects the variability of zooplankton and sea surface temperature, both of which are involved in air-sea exchanges of carbon dioxide. First, I examine the formation of spatial patterns in the distribution of Antarctic krill (*Euphausia superba*) resulting from social behavior. Turbulence of the flow is found to provide favorable conditions for the evolution social behavior in an idealized biological-physical model. Second, I analyze observations of sea surface temperature variability in the region of the Antarctic circumpolar current. Results suggest that propagating anomalies can be explained as a linear response to local atmospheric forcing by the Southern Annular Mode and remote forcing by El-Niño southern oscillation, in the presence of advection by a mean flow.

Thesis Supervisor: Glenn R. Flierl
Title: Professor of Oceanography

Acknowledgments

The work presented here is the result of collaborations with a number of people. I would like to thank them all: Arnaud Czaja for his guidance, John Marshall for his valuable support, Markus Jochum for his friendship. I am especially thankful to my advisor, Glenn Flierl, for giving me the opportunity to join his group and study ecosystems; his teachings have greatly contributed to my development as a researcher. I thank the Joint Program in Physical Oceanography at MIT and WHOI. Support from the Ocean Venture Fund and the Houghton Fund, which has allowed me to travel to conferences and summer schools, is gratefully acknowledged. Finally, I thank my classmates and friends from the Program in Atmospheres, Oceans and Climate for making my time here an enjoyable one.

Contents

List of Figures

Chapter 1

Introduction

Interactions between physical and biological processes in the Southern Ocean have significant impacts on local ecosystems as well as global climate. The production of organic carbon by photosynthetic plankton drives fluxes of CO_2 through the air-sea interface and cold, sinking waters carry a fraction of this carbon to the deep ocean, effectively sequestering it from the atmosphere. Plankton are, in turn, affected by the variability of the flow near the sea surface.

In this thesis I examine the mechanisms controlling the distribution of zooplankton and sea surface temperature in the Southern Ocean. Although the mechanisms involved are different, both large-scale temperature anomalies and smaller scale plankton patches contribute to the inhomogeneity of air-sea fluxes of carbon dioxide. Plankton patchiness is not explicitly resolved in global biogeochemical numerical models; however it is known to affect the oceanic productivity and its effect can be parameterized [Pascual et al., 2001].

In Chapter 2, I present a coupled biological-physical model of zooplankton competing for resources in a turbulent environment. Results from numerical simulations suggest that the tendency to form social aggregations can represent an advantage or a disadvantage for zooplankton, depending upon the flow conditions. I discuss how turbulent stirring and mixing, by supplying phytoplankton to clustered organisms,

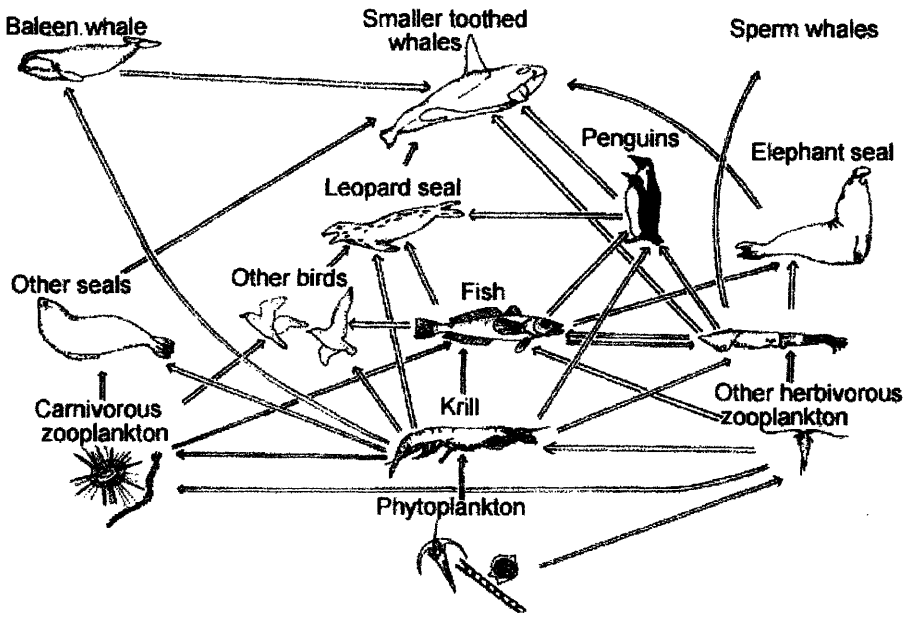

Figure 1-1: A simplified representation of the Antarctic ocean food web. The diagram highlights the central role of krill, which is the principal source of food for various species of whales, seals, fish and birds [Ward, 2005].

favors the evolution of grouping behavior. Antarctic krill, which are a central part of the Southern Ocean ecosystem (Figure 1-1), exhibit grouping behavior as well as response to large-scale and mesoscale ocean circulations. Recent observations have revealed the existence of aggregation patches of Antarctic krill with horizontal scale of 100 m to 1 km, and densities on the order of 100 individuals/m^3. These densely populated patches are found mostly in turbulent circulation features such as small-scale jets and eddies which supply food to the krill.

In Chapter 3, I investigate the role of mean ocean circulation in the generation and propagation of temperature anomalies at the sea surface. The Antarctic Circumpolar Current (ACC) is the principal dynamical feature in the Southern Ocean (Figure 1-2); flowing eastward around Antarctica, it advects water properties under a stormy atmosphere. This stochastic forcing is found to induce low-frequency variability in sea surface temperature (SST). Observational data shows that SST anomalies are

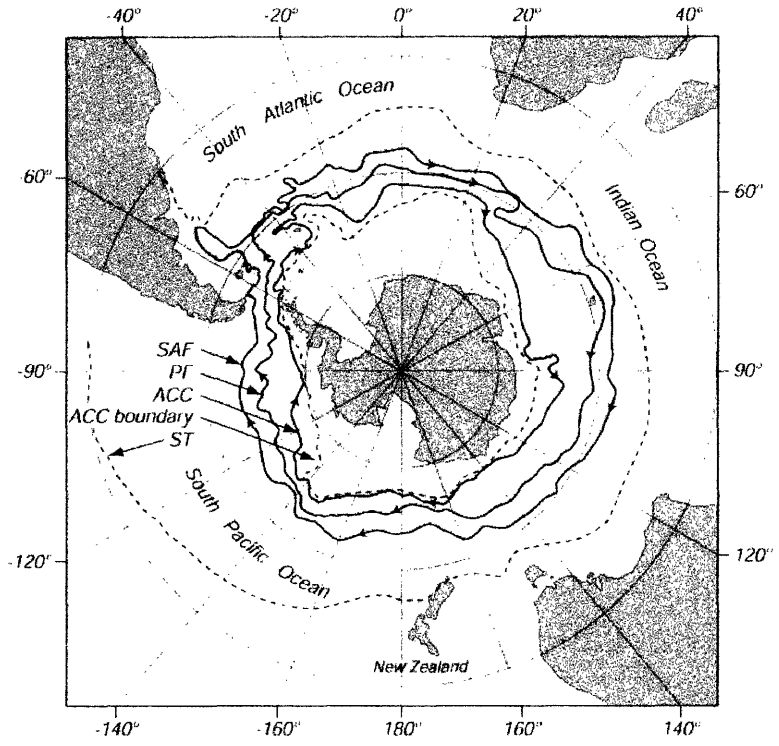

Figure 1-2: A map of the Southern Ocean, showing the location of the Antarctic Circumpolar Current. The boundaries of the current are indicated by dashed lines. The map also shows the position of the Subantarctic front (SAF), polar front (PF) and southern ACC front (ACC). From Whitworth [1988]

generated mainly in the South Pacific basin through heat fluxes driven by the El-Niño-Southern Oscillation and the Southern Annular Mode. I present a simple model of SST forced by the observed heat fluxes and advected by the mean geostrophic flow of the ACC, and show that it reproduces well the first-order features of observed temperature variability.

Chapter 2

Evolution of grouping behavior in krill

Verdy, A. and G. Flierl

Deep-Sea Res. II, submitted (2006)

Turbulent motions in the ocean affect the distribution of zooplankton. Despite the dispersion resulting from stirring and mixing by the flow, coherent groups are observed in populations of organisms with social behavior, notably Antarctic krill. We employ a biological-physical model to investigate the evolutionary advantages associated with the formation of social aggregations, under different flow conditions. The model simulates the transmission and slow mutation of a gene controlling the aggregation behavior; natural selection determines whether the grouping or non-grouping type becomes dominant. It is found that grouping behavior can evolve when reproduction is strongly density-dependent and mixing occurs rapidly enough for resources to remain available to the clustered organisms. Turbulent advection prevents the grouping type from becoming dominant if the flow shear is strong enough to disrupt the patches; otherwise the aggregated zooplankton benefits from enhanced diffusion of resources by the turbulent flow.

2.1 Introduction

Zooplankton aggregation occurs as the result of both biological and physical processes. In the ocean, the density distribution of plankton is influenced by circulation patterns such as mesoscale vortices [Abraham, 1998; Flierl and McGillicuddy, 2002; Lévy and Klein, 2004; Pasquero, 2005] and fronts [Epstein and Beardsley, 2001; Franks, 2002; Genin et al., 2005]. The behavior of individuals responding to their environment also plays a significant role in the generation of dense, quasi-horizontal patches of zooplankton commonly called swarms [Folt and Burns, 1999]. Physical and chemical cues can trigger collective movements in a population, or the cue can be the density of conspecifics, in which case the tendency to form groups is referred to as *social behavior.*

A variety of mathematical models have been employed to describe the mechanisms responsible for the development of swarms in populations of organisms with social behavior. Mechanisms involving a balance between attractive and diffusive forces lead to the formation of cohesive groups [Okubo, 1980; 1986; Flierl et al., 1999; Zhou and Huntley, 1996]. Even in the absence of environmental variability, groups can form spontaneously when swimming velocities are, on average, directed up the gradient of density and are strong enough to overcome dispersion by the flow and by the randomness of individual motion. Schools develop when organisms also tend to align their orientation with close-by neighbors [Flierl et al., 1999].

From an evolutionary point of view, the reasons for self-organized patchiness are not well known. The dynamics of groups have important ecological consequences [Levin, 1994; Parrish and Edelstein-Keshet, 1999]; however the nonlinear nature of predator/prey and competitive interactions makes it hard to predict whether grouping will increase or decrease individual fitness. In some cases, aggregation is thought to be an anti-predator strategy [Hamilton, 1970]. Other advantages include improvement of foraging success and mating probability; these benefits are traded-off with the costs of competition for resources between group members [Parrish and Edelstein-Keshet,

1999]. Persistent groups are also observed to attract predators [De Robertis, 2002].

The costs and benefits of grouping will depend on environmental conditions. In this paper. we examine the effects of turbulent stirring and mixing on the competitive abilities of organisms with social behavior. Turbulent flows are associated with horizontal and vertical transport of resources in the euphotic zone, thus affecting ecosystem dynamics. Turbulence also causes merging and splitting of plankton aggregations [Flierl et al., 1999].

We employ a biological-physical model to investigate under what flow conditions does social behavior represent a favorable adaptation, and therefore can evolve in the population. The model simulates the transmission and slow mutation of a gene controlling aggregation behavior; natural selection determines whether the grouping or non-grouping type becomes dominant.

Our work is motivated by observations of Antarctic krill (*Euphausia superba*), which are a central part of the Southern Ocean ecosystem. These animals clearly exhibit aggregative and schooling behavior [e.g. Marr, 1962; Miller and Hampton, 1989] and, despite their large size, respond to large- and meso-scale circulations [Ashjian et al., 2004]. The observed variance spectrum of krill in the Southern Ocean is significantly flatter than that of phytoplankton or temperature in the same region, indicating the presence of fine-scale structure in the density distribution of krill [Weber et al., 1986]. Smaller zooplankton have variance spectra that lie between those of krill and phytoplankton [Mackas and Boyd, 1979].

The layout of the paper is as follows. The model equations are presented in Section 2.2, and analyzed in Sections 2.3.1-2.3.2. The impact of turbulent flow on the development of patches is investigated numerically in Section 2.3.3. In Section 2.4, we investigate the environmental conditions leading to the invasion of a non-grouping population by a grouping mutant. Conclusions are presented in Section 2.5.

2.2 Model formulation

The biological dynamics and motion of a single species of zooplankton is simulated in a 2-dimensional, periodic horizontal plane which represents the oceanic mixed layer. A continuum approach is used, where modeled fields are biomass densities rather than discrete numbers of individuals. In order to capture the effects of resource limitation, the dynamics of a phytoplankton are also simulated. Density-dependence of the zooplankton reproduction is taken into account, but predation by higher trophic levels is parameterized as independent of the zooplankton density.

2.2.1 Genetic model

We adopt a one-locus, two-allele model to simulate the transmission of a gene controlling social behavior. Of the three possible genotypes 00, 01 and 11, only the last one exhibits grouping behavior. Mendelian breeding is assumed (Table 2-1), although the possibility of spontaneous changes in the offspring's genotype is considered. These mutation events occur at a slow rate, with equal probability for both alleles, and affect a single allele at the time. If genetic differences did not affect survival, the population would thus slowly equilibrate to a 1:2:1 ratio of genotypes.

Expression of the genotype will presumably influence fitness, however, and affect the genotype frequencies. It is expected that grouping will enhance reproduction, while decreasing the availability of resources; the overall fitness is dependent on the

Table 2.1: Genotypes of offsprings

	00	01	11
00	00	$\frac{1}{2}$ 00+$\frac{1}{2}$ 01	01
01	$\frac{1}{2}$00+$\frac{1}{2}$01	$\frac{1}{4}$00+$\frac{1}{2}$01+$\frac{1}{4}$11	$\frac{1}{2}$01+$\frac{1}{2}$11
11	01	$\frac{1}{2}$01+$\frac{1}{2}$11	11

balance between these two effects. In our model, fitnesses are not explicitly specified; the relative success of the grouping and non-grouping types is determined by numerical simulations.

2.2.2 Ecosystem dynamics

A system of coupled differential equations describes the interactions between zooplankton (Z) and their food resource, phytoplankton (P):

$$\frac{dZ}{dt} = ag(P)ZH(Z) - mZ \equiv R_Z \tag{2.1}$$

$$\frac{dP}{dt} = rP\left(1 - \frac{P}{K}\right) - g(P)ZH(Z) \equiv R_P \tag{2.2}$$

where the mating probability is density-dependent:

$$H(Z) = \frac{Z}{c + Z} \tag{2.3}$$

Phytoplankton is assimilated with efficiency a, and grazed at a rate $g(P)$, which we choose to be a Holling type II functional response: $g(P) = \frac{P}{P+P_0}$, where P_0 is the half-saturation constant. We assume linear mortality rate m for the zooplankton and logistic growth for the phytoplankton, with r the growth rate and K the carrying capacity.

There is a positive correlation between the mating probability and the zooplankton biomass. The positive constant c ensures that the mating probability is always less than 1. For sparse populations, the zooplankton growth term $ZH(Z)$ behaves like a quadratic function; for large populations the growth term becomes a linear function of Z. Thus as the population decreases, its growth slows down, further decreasing the population density. This positive feedback, known as the Allee effect, can induce stochastic extinction of small populations [Boukal and Berec, 2002]. It may also provide an advantage to the grouping organisms.

In the case of Antarctic krill, mating involved direct contact between male and female organisms, thus it is likely that the process is density-dependent. The rectangular hyperbolic form of H that we choose emerges from considerations of probabilities of encounters during the reproductive period, competition for mates, or fecundity that depends on the mating frequency [Boukal and Berec, 2002].

2.2.3 Advection and diffusion

The equations describing the movements of organisms in the continuum approximation are derived in Flierl et al. [1999]. Zooplankton motion driven by attractive forces is expressed as an advection term, representing average swimming velocities, and a diffusion term representing randomness of individual displacements. Mixing occurring on small scales that are not resolved by the model is also parameterized as diffusion, and affects both the phyto- and zoo-plankton fields. For simplicity we will consider a unique value for the diffusivities of both species; this is equivalent to making the assumption that the random component of zooplankton motion is small. These diffusive and advective effects are added to the reaction terms given by equations (2.1-2.2).

The spatial distributions of biomass, $Z(\mathbf{x},t)$ and $P(\mathbf{x},t)$, are given by

$$\frac{\partial Z}{\partial t} = R_Z - \nabla \cdot [\mathbf{u}Z - \kappa \nabla Z] \tag{2.4}$$

$$\frac{\partial P}{\partial t} = R_P + \nabla \cdot [\kappa \nabla P] \tag{2.5}$$

∇ being the horizontal laplacian, $\mathbf{u}$ the swimming velocity, κ the diffusivity.

The average swimming velocity of zooplankton at a given location results from social behavior; for non-grouping organisms (genotypes 00 and 01), the movements are random and vanish on average ($\mathbf{u}$=0), but the grouping type 11 has a velocity

which depends on the local gradient in density:

$$\mathbf{u} = \nabla\phi \tag{2.6}$$

$$\phi = \iint W(\mathbf{x}')Z(\mathbf{x}+\mathbf{x}')d\mathbf{x}' \tag{2.7}$$

The function $\phi(\mathbf{x})$ represents the desirability of being at location $\mathbf{x}$; it is a weighted average of the density of zooplankton within the sensing radius of an individual. The weighting kernel W has a characteristic horizontal scale of L, and a magnitude proportional to the swimming speed. We choose a function that is negative at short distance, becomes positive, has a maximum at L and then vanishes as the distance increases; this geometry accounts for the finite area of attraction and the repulsion at short distances (Figure 2-1).

It should be noted that (2.4) is computed for each of the zooplankton genotypes, with advection and diffusion acting only on the type considered; but the density in (2.7) refers to the total zooplankton population, as organisms with social behavior are attracted not only to their type but to all conspecifics. The system described above is solved numerically using a finite-differences scheme.

2.2.4 Turbulent stirring

To represent turbulent advection, we use a formalism akin Pierrehumbert [2000]. The grid underlying the numerical model is viewed as a lattice, whose elements are displaced by a non-divergent flow. Displacements are constrained to be equal to a multiple of the grid size (Δx) so that the lattice isn't deformed under the flow. With this constraint, the turbulent advection scheme does not contribute to diffusion. The stirring will induce sharper gradients in the fields, though, and thus enhance diffusion at small scales which is included in the differential equations (2.4-2.5). The algorithm is iterated in two steps. Every odd time step, the zonal displacement (δ_x) is applied

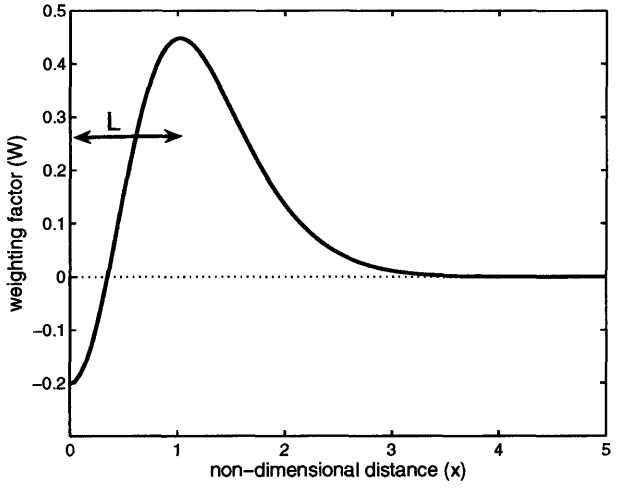

Figure 2-1: Weighting factor accorded to neighboring organisms as a function of their distance from zooplankton located at x=0, as they adjust their velocity to move up the gradient of neighbors density: $W(x) = exp(-x^2/2) - exp(-2x^2)$. Distances are expressed in units of L, the characteristic perception length scale. The sensing radius has an approximate value of 2; individuals within the sensing radius are perceived by zooplankton with social behavior. Positive weighting indicates attraction to neighbors. Repulsion at short distance prevents over-crowding.

and every even time step, the meridional displacement (δ_y) is. The equations are

$$\delta_x = round\left[\frac{\delta_0}{\Delta x} sin\left(\frac{2\pi}{W} y + \theta_u\right)\right] \Delta x \tag{2.8}$$

$$\delta_y = round\left[\frac{\delta_0}{\Delta x} sin\left(\frac{2\pi}{W} x + \theta_v\right)\right] \Delta x \tag{2.9}$$

where the phase θ_u (similarly for θ_v) has a random component

$$\theta_u(t + 2\Delta t) = \theta_u(t) + R \tag{2.10}$$

with W the width of the domain, δ_0 the magnitude of the displacements, R a random number varying between 0 and 2π; the terms between brackets are rounded to the nearest integer.

Δt is the time step for the turbulent advection scheme, and might differ from the

time step used to solve the partial differential equations. The velocity of the flow is proportional to the ratio $\delta_0/\Delta t$, and can be controlled by varying either of these parameters.

2.3 Development of patches

In this section we will examine the conditions leading to the formation of zooplankton patches. First, we will adimensionalize the model equations, to facilitate the stability analysis. We will then proceed to numerical simulations.

2.3.1 Non-dimensional system of equations

We scale time by r^{-1}, lengths by L, phytoplankton and zooplankton biomass by P_0 and $P_0 r/g$, respectively. Some non-dimensional numbers are introduced to replace the parameters in the reaction terms: $\gamma = ag/r$, $\mu = m/r$, $\chi = K/P_0$; λ is simply the constant c redefined. Following Flierl et al. (1999), we scale ϕ by κ, velocities by κ/L, and W by $W_0 \equiv \iint W/L^2$.

The non-dimensional equations are

$$\frac{\partial Z}{\partial t} = \gamma G - \mu Z - \tau \nabla \cdot [\mathbf{u} Z - \nabla Z] \tag{2.11}$$

$$\frac{\partial P}{\partial t} = P\left(1 - \frac{P}{\chi}\right) - G + \tau \nabla \cdot [\nabla P] \tag{2.12}$$

where

$$G \equiv \frac{P}{P+1} \frac{Z^2}{\lambda + Z} \tag{2.13}$$

and, for individuals with social behavior,

$$\mathbf{u} = \nabla\phi \tag{2.14}$$

$$\phi = \epsilon \iint W(\mathbf{x}')Z(\mathbf{x}+\mathbf{x}')d\mathbf{x}' \tag{2.15}$$

Two important non-dimensional parameters appear. The first one is ϵ, the Peclet number, comparing movement rates to diffusive rates [Flierl et al., 1999]. Defining the characteristic swimming speed $u_{bio} = gP_0W_0L/r$, we have $\epsilon = u_{bio}L/\kappa$; this parameter is a measure of the strength of social behavior. The second parameter is τ, the ratio of the timescale inherent to the movements to the biological timescale: $\tau = \kappa/L^2r$.

In this study, we choose the biological parameters to be $\gamma = \lambda = 1$, $\chi = 0.5$ and $\mu = 0.1$. These values are somewhat arbitrary, and have been chosen because they are associated with stable and steady coexistence of phyto- and zoo-plankton. In the absence of motion, the P and Z concentrations at equilibrium are found by equating (2.11) and (2.12) to 0, with $\tau = 0$. For the parameter values above, there is a single stable equilibrium for which both species coexist, and the equilibrium values in non-dimensional units are

$$P^*, Z^* = \{0.22, 1.22\} \tag{2.16}$$

If the distribution of plankton were uniform in space, it would remain at equilibrium. However, spatial patterns will appear in the zooplankton distribution when the tendency to swim up the gradient of neighbor density is sufficient to compensate diffusion resulting from the flow.

2.3.2 Self-organized patchiness

We now examine the linear stability of the dynamical system (2.11-2.15) around the equilibrium biomass (2.16). Instability implies that groups will form spontaneously

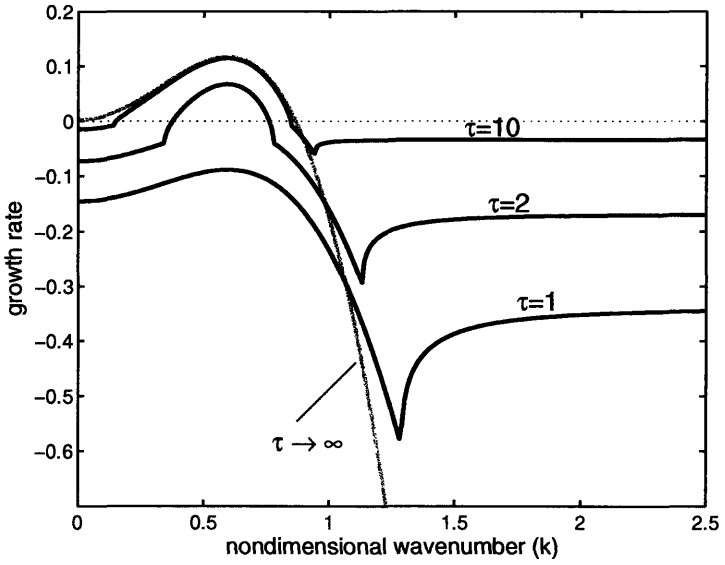

Figure 2-2: Linear growth rate of small perturbations around the equilibrium biomass versus the wavenumber of the perturbations, for $\epsilon = 1.4$ and for different values of τ. In a uniform distribution of zooplankton, random variations will spontaneously lead to the formation of patches, if there is positive growth somewhere along the wavenumber spectrum. The gray line shows the case where zooplankton motion is decoupled from biological activities, as calculated in Flierl et al. (1999). Rates are normalized by $1/\tau$. When biological and movement occur at similar rates, the stability condition can be changed from considering biological activities; this is the case here for $\tau = 1$ (growth rate always negative). As the motion becomes faster, the growth rates for the cases with and without biology are almost indistinguishable in the region of instability (positive growth).

in a population of zooplankton that is initially uniformely distributed in space. Small perturbations in the density field will be damped if the system is stable, but will grow in time and become dense patches if it is unstable. Perturbations can be expressed in terms of Fourier modes: $Z' = Z'exp(i\mathbf{k} \cdot \mathbf{x})$ and $P' = P'exp(i\mathbf{k} \cdot \mathbf{x})$, where $\mathbf{k}$ is the horizontal wavemumber.

In order to find an expression for the stability criterion, turbulent advection will be neglected in this analysis. We begin with the assumption that the zooplankton population is composed entirely of individuals with social behavior. The jacobian of

(2.11-2.12) evaluated at (2.16) is then

$$\mathbf{J}=\begin{bmatrix} \gamma N-\mu-\tau|\mathbf{k}|^2(\epsilon\hat{W}Z^*-1) & \gamma M \\ N & 1-\frac{2P^*}{\chi}-M \end{bmatrix} \tag{2.17}$$

where we have defined

$$M \equiv G\left(\frac{1}{P^*}-\frac{1}{P^*+1}\right) \tag{2.18}$$

$$N \equiv G\left(\frac{2}{Z^*}-\frac{1}{\lambda+Z^*}\right) \tag{2.19}$$

and the Fourier transform of W is

$$\hat{W}=\hat{W}(\mathbf{k}) \equiv \iint W e^{i\mathbf{k}\cdot\mathbf{x}'}d\mathbf{x}' \tag{2.20}$$

Eigenvalues of the jacobian matrix give the linear growth rate of perturbations; if at least one of them is positive, the system is unstable. Rather than writing the complicated expression for the eigenvalues, we have computed them numerically. The leading eigenvalue is plotted in Figure 2-2 as a function of the wavenumber.

In the limit $\tau \to \infty$, all but one term in (2.17) become negligible; when motion is very fast compared to growth and mortality, coupling to phytoplankton can be ignored. The system is reduced to a 1-dimensional equation, for which the stability criterion is derived in Flierl et al. [1999, section 4.4]. Instability occurs for $\epsilon Z^*\hat{W} \geq 1$, where Z^* is the mean zooplankton concentration ($\bar{\rho}$ in Flierl et al. [1999]). Biological terms increase the stability (Figure 2-2).

Assuming now that only a fraction of the population exhibits social behavior, what is the condition for the development of patches? In the linear stability problem, the presence of non-grouping organisms does not come into play and can thus be ignored. It is sufficient to multiply Z^* in (2.17) by f, the fraction of grouping type, to find the new stability criteria. For a given value of ϵ, there is a minimum density of grouping

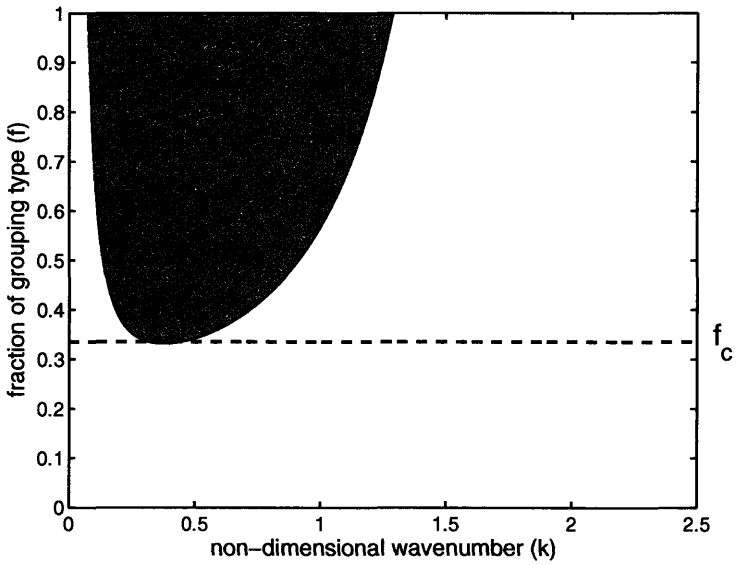

Figure 2-3: Stability of the ecosystem model as a function of the wavenumber of perturbations, and the fraction of grouping organisms in the population. Parameters are $\epsilon = 3$, $\tau = 10$. The shaded zone indicates positive growth of the perturbations, and thus instability which will lead to the formation of self-organized patches. Low numbers of individuals with social behavior are more stable. We note that there is a critical fraction (f_c) below which patchiness does not form.

organisms fZ^*required for instability. Constraining Z^* to its value (2.16), we define f_c as the critical fraction below which there is no spontaneous formation of patches. An example of the stability of the ecosystem versus f and the wavenumber is shown in Figure 2-3. Because of linearity, f_c varies with the grouping parameter such as to keep their product $f_c\epsilon$ constant.

The total population size does have an effect on the stability, but only via higher order terms. These nonlinear effects are noticeable in the numerical simulations. To minimize discrepancies with our analytical predictions, we initialize the model with spatial perturbations in the 11-type zooplankton only, neutralizing the effects of non-grouping organisms on the development of patches by making them perfectly homogeneously distributed.

2.3.3 Numerical simulations

Linear growth rates calculated above apply to perturbations when their amplitude is small. As the perturbations get larger, nonlinearities become increasingly important; eventually they contribute to stopping the growth mechanism. The final distribution of biomass is obtained more easily numerically than analytically. For the simulations we consider a square grid of non-dimensional width $W = 30$ and grid space $\Delta x = 0.25$; the time step varies between 10^{-3} and 10^{-4} depending on the parameters.

For $\epsilon = 1.4$, $\tau = 10$ and $f = 1$, the condition for instability is satisfied so that patches are expected to form (Figure 2-1); indeed, numerical simulations show that small deviations from the equilibrium zooplankton biomass grow into well defined groups, as illustrated in Figure 2-4. Initially, the scale of patchiness is determined by the wavenumber that has the highest linear growth rate, but as they get denser patches tend to merge, so the patchiness shifts to larger scales.

The fully developed groups have peak densities of roughly 30 times the mean density, and a diameter of $3 - 4L$. These characteristics vary slightly for different values of ϵ, larger values leading to the formation of denser, narrower patches.

Numerically, we can also investigate the impacts of turbulence on the development of patches. When the zooplankton field is advected by a turbulent flow, the resulting streakiness enhances diffusion, which acts against the formation of social aggregations. A strong flow will thus prevent groups from forming. Patchiness can develop if the flow is weak, however, as shown in Figure 5a. Turbulent advection in that case is sufficiently slow that zooplankton with social behavior can overcome the diffusion resulting from the flow.

Besides slowing down the initial growth of perturbations, we observe that turbulent flow induces collisions between patches. When two patches come near to each other, they permanently merge; after a finite amount of time there is only one dense patch in the domain. In our model, shear associated with the flow does not break fully-developed groups apart. When the shear is strong, patches simply do not form,

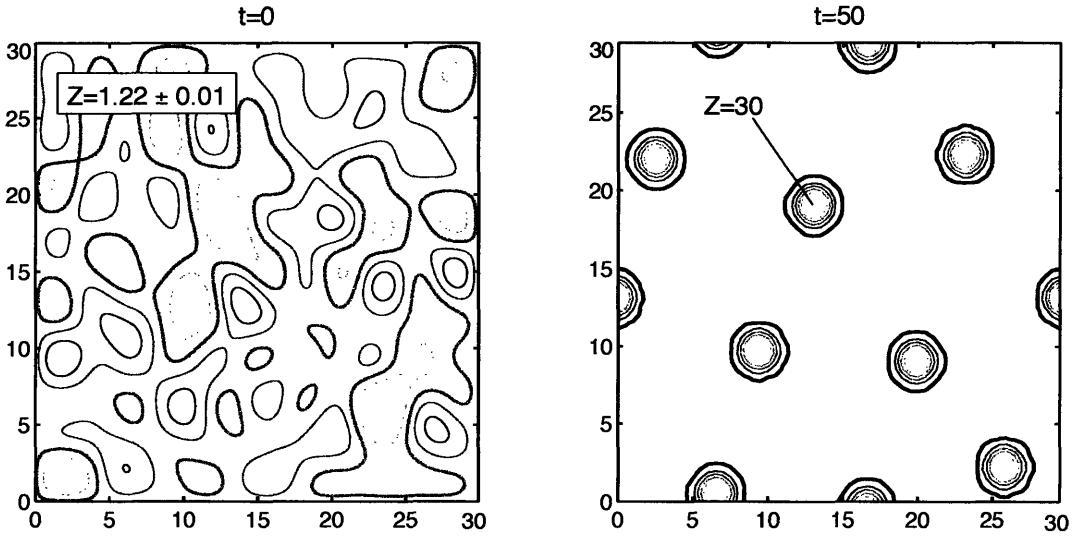

Figure 2-4: Zooplankton density in the horizontal plane. Biomass is initially uniformly distributed, with small perturbations (left); patches form spontaneously (right). In the left panel, contour interval is 0.005; the equilibrium density $Z^* = 1.22$ is shown by a thicker contour. In the right panel, the contour interval is 5; the zero contour is thicker. Patches have a horizontal scale proportional to the length L, which scales the spatial dimensions. All units are non-dimensional; parameters are $\epsilon = 1.4$, $\tau = 10$.

as shown in Figure 5b. In that case, the zooplankton field eventually becomes uniformly distributed in space.

To quantify the patchiness, we define an index

$$\tilde{p} = \frac{\iint \left(Z(\mathbf{x}) \cdot \iint_{-1}^{1} Z(\mathbf{x}+\mathbf{x}')d\mathbf{x}' \right) d\mathbf{x}}{4\left(\iint Z(\mathbf{x})d\mathbf{x}\right)^2 / W^2} - 1 \tag{2.21}$$

which compares the density of individuals within an area L^2 to the density expected if organisms were uniformly distributed.

The index vanishes for a well-mixed field; its value increases as patches form and merge (Figure 2-5a). In the strongly-turbulent environment of Figure 2-5b, the index is small at the beginning of the simulation and further decreases as the density is mixed by the flow. However, the zooplankton field remains spatially more intermittent

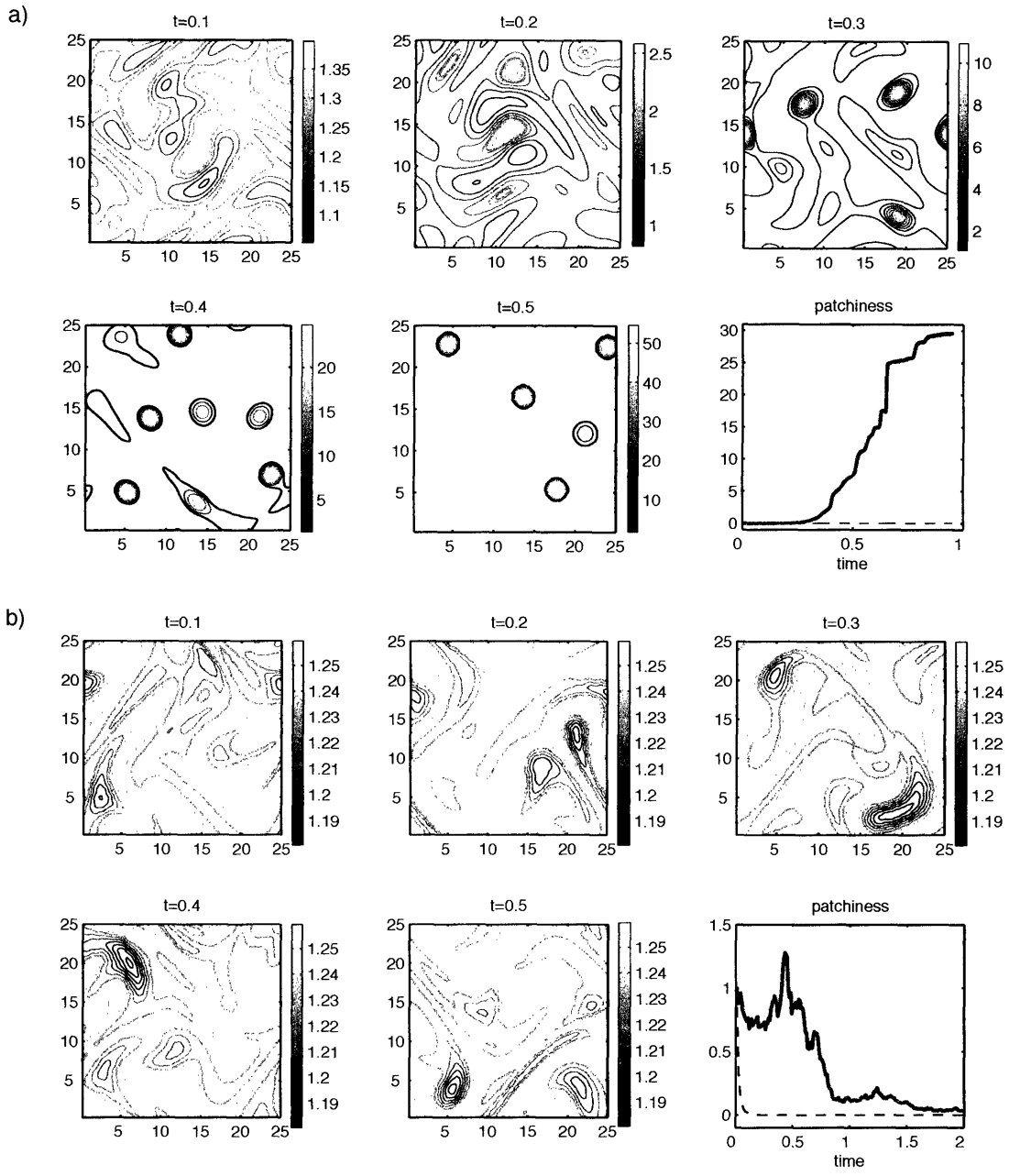

Figure 2-5: Effect of turbulent advection on the development of patches in a population of zooplankton with social behavior, $\epsilon = 5$. a) weak flow, $\delta_0/\Delta t = 25$: groups form and merge. The last panel shows an index for patchiness as defined in (21), increasing in time. b) strong flow, $\delta_0/\Delta t = 150$: horizontal shear prevents the development of patches. Stirring and mixing homogenize the zooplankton distribution, which for some time remains spatially more intermittent than a passive scalar field. The last panel shows the index for patchiness normalized by the value at t=0; solid curve is for zooplankton with social behavior, dashed curve is for a passive tracer. The thicker contour indicates the equilibrium density, $Z^* = 1.22$.

than a passive scalar field under the same flow conditions, as indicated by comparison of their respective patchiness indices.

2.4 Conditions for dominance of the grouping type

In this section, we examine the conditions that determine whether the grouping or non-gouping type will be a better competitor. We proceed through numerical simulations. The scenario we consider is the following: in a population of non-grouping homozygotes (genotype 00), a mutant allele is introduced. The reproductive and competitive abilities of the grouping and non-grouping types determine the final ratio of genotypes in the population.

Initially, the abundance of the new genotypes 01 and 11 increases through mutations only since the number of grouping organisms is below the critical fraction for patch formation. All types then have the same fitness. When the fraction of individuals with social behavior reaches f_c, however, patchiness starts appearing. Instead of simulating the mutation process, we start the simulation with a fraction f_c of type 11 in the population; the fraction of other genotypes is chosen accordingly so that, without mutations, the ratio of types would be constant. It is assumed that ecological processes occur much faster than mutations, which can therefore be neglected in the simulations.

2.4.1 Mixing and stirring effects

Once again it is useful to consider first a case without turbulent advection, in order to get a sense of what parameters are influencing the competitive abilities of both types. Figure 2-6 shows the two possible outcomes of the competition. For the parameters $\epsilon = 5$, $\tau = 10$, the non-grouping type is dominant; but increasing the value of τ leads to replacement of the resident population by the grouping type. Simulations with different parameters consistently show that there is a critical value of τ above which

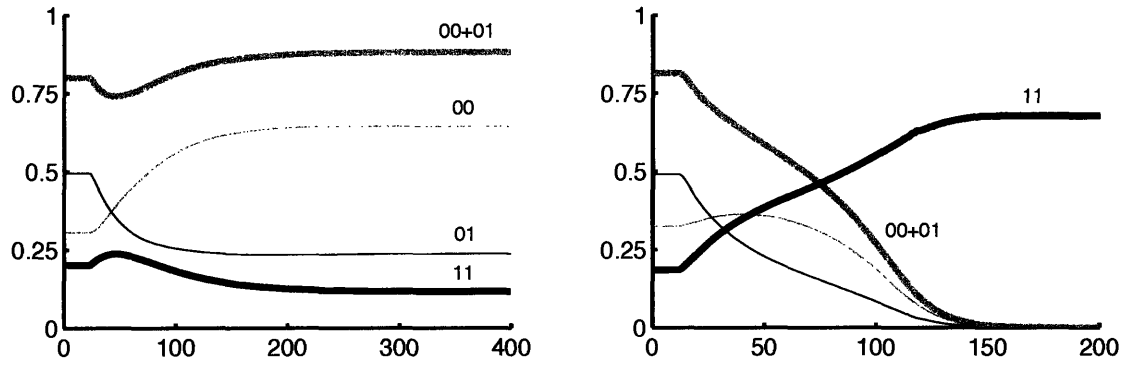

Figure 2-6: Frequency of zooplankton genotypes versus time; $\epsilon = 5$. Left: $\tau = 10$, the grouping types does not invade, but remains in the population at low frequency. Right: $\tau = 25$, the grouping type invades, and non-grouping types disappear from the population. Thin gray and black lines show the genotypes 00 and 01 respectively, while the thick gray line shows the sum of non-grouping types; thick black line shows the grouping genotype, 11. Initially the grouping type represents a fraction f_c of the population.

the grouping type dominates; moreover, we find that this critical value is independent of the grouping parameter.

These results highlight the importance of food availability for the survival of aggregated zooplankton. In our model, increasing τ has the effect of enhancing mixing, by increasing diffusion rates while keeping biological rates constant. Thus resources are supplied faster to clustered organisms whose grazing rate is unchanged, partially relieving the food limitation.

Varying ϵ does not affect the stability criterion, since there is a simultaneous change in f_c (Section 2.3). By definition of f_c, instability occurs for a single value of $\mathbf{k}$. This wavenumber, which determines the scale of growing patches, is the same for all pairs of values of ϵf_c. The density profile in aggregations is thus almost unaffected by the parameter ϵ; as a result, the availability of food is also unaffected.

Turbulent advection affects the competition between the grouping and non-grouping types, by contributing to supplying resources to clustered organisms. Strong stirring has been shown to prevent patches from forming (Section 2.3), but when zooplankton

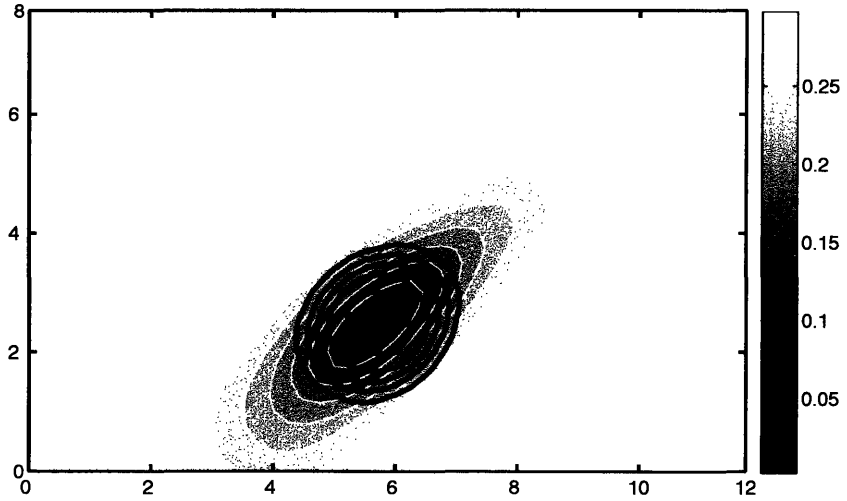

Figure 2-7: Contours of zooplankton biomass, black lines, superimposed on the phytoplankton field, gray shades. This shows stirring of resources by the turbulent field, for parameters $\epsilon = 5$, $\tau = 10$, $\delta_0 = 1$ and $\Delta t = 10^{-2}$.

groups form in a weakly turbulent flow, they resist the shear of that flow. Shear affects the distribution of phytoplankton, however; grazing creates regions of depleted resources, coinciding with the location of the zooplankton patches. In the model, phytoplankton is passively advected, thus depleted areas are subject to deformation by the flow. The resulting elongation enhances the gradient in phytoplankton density, which accelerates diffusion of resources toward aggregated zooplankton, as shown in Figure 2-7.

Comparison of Figures 2-6a and 2-6b reveals differences in the time evolution of the ratio of genotypes during the competition. When the grouping type wins the competition, the types 00 and 01 are eliminated from the population; only the mutant allele remains in the gene pool. In cases where the non-grouping type dominates, however, the type 11 does not disappear from the population. Since the mutant heterozygote does as well as the resident, both alleles remain in the gene pool; grouping offsprings are produced from mating between heterozygotes (Table 2-1). After a tran-

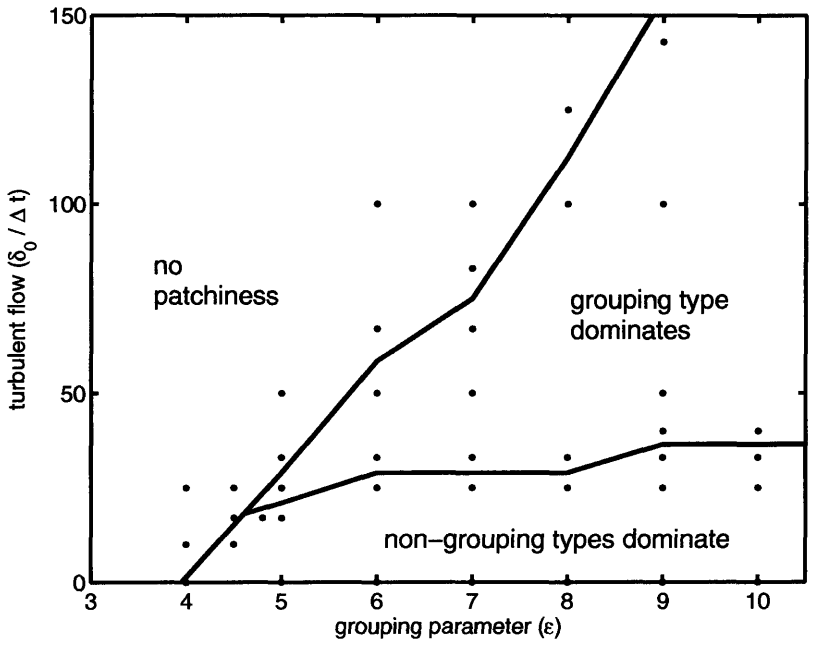

Figure 2-8: Bifurcation diagram showing the outcome of the competition between grouping and non-grouping types, when the mutant allele is introduced at low density in a resident population of non-grouping organisms. The grouping parameter and strength of turbulent flow are varied; τ is kept constant ($\tau = 10$). Except in the region labeled "no patchiness", zooplankton with social behavior spontaneously assemble in dense groups. Without turbulent advection ($\delta_0/\Delta t = 0$), they are outcompeted by the non-grouping types and remain a small fraction of the population. Weak flows do not affect the outcome of the competition, but under more turbulent flows the grouping type becomes a better competitor and replaces the non-grouping resident organisms. Black dots indicate parameter values for which numerical simulations were performed.

sient increase in the number of grouping zooplankton, their frequency decreases until they constitute only a small fraction of the total population; however that remaining fraction is still found in aggregations.

2.4.2 Bifurcation analysis

We limit the size of the domain such that only one group can form in the absence of turbulent stirring. Merging of patches resulting from collisions in a turbulent environment reduces the competitive ability of the grouping type, for the width and density of groups increases and consequently resources are depleted faster.

Numerical simulations show that turbulent stirring and mixing can lead to invasion by the grouping type, for parameters that would not have allowed for invasion in the absence of flow. For example, with $\epsilon = 5$, $\tau = 10$ and $\delta_0 = 0$ the non-grouping type wins the competition, see Figure 2-6a; but when $\delta_0 = 1$ then the grouping type dominates.

The outcome of the competition is examined in parameter space (Figure 2-8). For small values of ϵ or large values of the flow strength, the critical fraction for the formation of patches is larger than 1/4, so it will not be reached by mutation alone; all types will be uniformly distributed in space and the final ratio of types will be 1:2:1 in these cases. When the social behavior is strong enough for patchiness to develop, the winning type depends on the conditions.

Figure 2-8 shows the positive impact of turbulent stirring and mixing on the invasibility by the grouping type. For the parameters chosen, the grouping type does not invade in the absence of advection, and weak flow does not change the outcome of the competition. As the strength of the flow is increased, grouping becomes an advantageous strategy. These results suggest that turbulent environments can promote the evolution of social behavior in a zooplankton population.

2.5 Conclusions

In aquatic environments, the spatial distribution of zooplankton is controlled by the behavior of individuals and by the variability of the flow. Here we have studied how the interplay between behavior and physics affects the survival of organisms that tend

to form social aggregations. This issue is important for understanding the distribution of krill, which exhibit social behavior as well as response to large-scale and mesoscale circulations in the ocean.

We have examined under what environmental conditions grouping behavior represents an advantage for zooplankton, when the factors to balance are competition for resources and mating success. Our biological-physical model explicitly includes a phytoplankton population, in order to capture the effects of resource limitation on the competition between organisms with and without grouping behavior. It is found that disadvantages associated with depleted resources within zooplankton aggregations can be balanced by the abundance of mates. When there is an Allee effect in reproduction, that is when probability of mating is positively correlated with density, the grouping type dominates if phytoplankton diffusion is sufficient. Turbulent environments are thus favorable to the evolution of the social behavior, as stirring and mixing by the flow provides resources to the clustered zooplankton. When the turbulent advection is larger than a critical value, however, patches cannot develop and, as a result, the behavior does not evolve.

Many processes contributing to krill patchiness have not been considered in this study. Diurnal cycles of vertical migration keep organisms at a common depth and help maintaining coherent groups [Zhou and Dorland, 2004]. Predation by whales, penguins, and other large animals is likely to be density-dependent and to play a role in the evolution of social behavior. If the probability of being preyed upon decreased with the local density, then aggregation would positively affect the survival rate, leading to the possibility of the grouping type outcompeting non-grouping organisms even in the absence of an Allee effect in the reproduction function. An improved version of the model would also account for the tendency of individuals to align their orientation with their neighbors, a behavior responsible for the formation of schools, as opposed to "patches", in adult Antarctic krill.

Chapter 3

Sea Surface Temperature Variability Along the Path of the Antarctic Circumpolar Current

Verdy, A., J. Marshall and A. Czaja

Journal of Physical Oceanography, in press (2006)

The spatial and temporal distribution of sea surface temperature (SST) anomalies in the Antarctic Circumpolar Current (ACC) is investigated, using monthly data from the NCEP-NCAR Reanalysis for the period 1980-2004. Patterns of atmospheric forcing are identified in observations of sea level pressure and air-sea heat fluxes. It is found that a significant fraction of SST variability in the ACC can be understood as a linear response to surface forcing by the Southern Annular Mode (SAM) and remote forcing by ENSO. The physical mechanisms rely on the interplay between atmospheric variability and mean advection by the ACC. SAM and ENSO drive a low-level anomalous circulation pattern localized over the South Pacific, inducing surface heat fluxes (Fs) and Ekman heat advection (Fek) anomalies. A simple model of SST propagating in the ACC, forced with heat fluxes estimated from the Reanalysis,

suggests that Fs and Fek are equally important in driving the observed SST variability. Further diagnostics indicate that SST anomalies, generated mainly upstream of Drake Passage, are subsequently advected by the ACC and damped after a couple of years. We suggest that SST variability along the path of the ACC is largely a passive response of the oceanic mixed layer to atmospheric forcing.

3.1 Introduction

In the Southern Ocean, sea surface temperature (SST) anomalies are observed to propagate eastward; it has been suggested that the signal encircles the globe 8 to 10 years [White and Peterson, 1996]. This low-frequency variability arises from mechanical and thermodynamic forcing at the air-sea interface. Mechanisms controlling the spatial and temporal scales of SST variability in the Southern Ocean are not well understood, nor is the extent to which coupled ocean-atmosphere interactions play a role.

Remote forcing by El Niño-Southern Oscillation (ENSO) has been proposed as a trigger of SST variability [White and Peterson, 1996; Cai and Baines, 2001], through teleconnections with the tropics. ENSO has also been linked to sea ice extent variability around Antarctica [Yuan and Martinson, 2000]. In contrast, based on the result of their numerical model, Hall and Visceck [2002] have argued that much of the variability in the Southern Ocean, including SST, is forced locally by the Southern Annular Mode (SAM), a dominant source of atmospheric variability in the Southern Hemisphere.

The role of ocean dynamics in the generation and maintenance of SST anomalies has also been examined (see, for example, Haarsma et al. [1999]). The presence of the Antarctic Circumpolar Current (ACC), a strong eastward flow in a zonally periodic domain, can lead to interesting dynamics. Away from the frontal jets, the speed of the flow in the ACC is similar to the propagation speed of SST anomalies, and it is

tempting to believe that the ACC is involved in carrying the anomalies. However, whether the signal will propagate significant distances depends on the rates of advection and damping. Decay of SST anomalies through interaction with the atmosphere typically occurs over a period of a few months [Frankignoul,1985]. This implies that visual propagation of the signal would not be possible without a mechanism that maintains the anomalies in the face of damping.

Two explanations have been put forward for the observed persistence of SST variability: the first is based on the interplay between stochastic atmospheric forcing and ocean advection [Haarsma et al., 2000; Weisse et al., 1999], while the second relies on the growth of coupled modes of the ocean-atmosphere system [Qiu and Jin, 1997; White et al., 1998; Talley, 1999; Goodman and Marshall, 1999; 2003] that act against damping processes, thus increasing the longevity of SST anomalies. The main difference between the two mechanisms lies in the role of the ocean, whether passively responding to atmospheric forcing or actively involved in the ocean-atmosphere coupling.

The hypothesis of an active role for the ocean was motivated by the observation of a phase-locked propagation of sea level pressure (SLP) and SST anomalies [White and Peterson, 1996]. The phenomenon was dubbed the Antarctic Circumpolar Wave (ACW) by White and Peterson [1996] due to the apparent periodicity of the signal. SLP anomalies are observed to lag SST anomalies by 1/4 wavelength. This configuration suggests that atmospheric circulation is dynamically affected by oceanic feedbacks, in such a way that the anomalies grow in time. Following the idea of mid-latitude ocean-atmosphere coupling of Latif and Barnett [1994] , White et al. [1998] proposed a mechanism in which SST anomalies are amplified by meridional advection of warm / cold air resulting from vortex stretching over warm / cold water. In the two-layer ocean model of Qui and Jin [1997], the equivalent barotropic response of the atmosphere induces a wind stress curl downstream of SST anomalies, which are then reinforced though Ekman pumping in the ocean. Such scenarios involving ocean

feedbacks are controversial, as there is little observational evidence for extra-tropical coupled modes. Cases where the oceanic feedbacks have a considerable impact on the local climate are more commonly found in the tropics [Kushnir et al., 2002].

Mechanisms which do not require ocean-atmosphere coupling have also been put forward to interpret interannual SST variability. The analytical model of Saravanan and McWilliams [1998] shows that in the presence of a mean oceanic flow, it is possible to obtain decadal variability and propagation in the SST signal as a passive response to atmospheric forcing. The theory is based on the idea of stochastic climate model proposed by Hasselmann [1976] : low-frequency variability arises in the ocean from a slow response to random atmospheric forcing. If an advective ocean interacts with a spatially fixed forcing which is stochastic in time, a preferred timescale will be excited in the ocean, determined by the ratio of the length scale of the forcing and the speed of the mean flow. Saravanan and McWilliams [1998] explained decadal variability in the North Atlantic as a result of this "advective resonance" mechanism, where SST anomalies advected by the Gulf Stream interact with a dipole pattern of atmospheric forcing, identified with the North Atlantic Oscillation (NAO). In the Southern Ocean, one can think of a similar set of circumstances, in which advection by the ACC combined with standing patterns of atmospheric forcing associated with -for example- ENSO and SAM, lead to decadal signals.

The advective resonance mechanism can explain the ACW-like variability in the models of Weisse et al. [1999] and Haarsma et al. [2000]. In these numerical experiments, it is found that SST variability is excited by the dominant modes of variability in the atmosphere, which appear to have a wavenumber 2 or wavenumber 3 spatial pattern. The authors do not specifically identify the source of atmospheric variability behind these forcing patterns. Stochasticity of the forcing is a key element of the mechanism: there exists a frequency for which, by the time it takes an SST anomaly to travel from one pole of the forcing to the next, the forcing has reversed polarity, so that the anomaly created initially gets amplified. This process competes against

damping of the anomalies, and is responsible for their apparently long persistence. It results in a visual propagation of the SST signal, in the direction of ocean advection. Advective timescales become amplified in the SST spectrum; the spectrum is easily found analytically for a sinusoidal spatial pattern [Saravanan and McWilliams, 1998]; Scott [2003] solved it for a periodic domain.

The motivation for the present study is to understand the physical mechanisms leading to observed interannual SST variability in the Southern Ocean. Our goal is to assess the role of ocean dynamics and atmospheric forcing; in particular we focus on the role of ENSO and SAM, the former because of its well-documented role in oceanic variability especially in the tropical Pacific but also in the tropical Atlantic [Czaja et al., 2002] and North Pacific [Alexander et al., 2002]; the latter because it is dynamically similar to the NAO, which also is known to drive variability in the ocean [Marshall et al., 2001]. We wish to put forward the view that SST variability along the path of the ACC can simply be understood as a passive response of the ocean mixed layer to SAM and ENSO forcing. Mechanisms involve primarily mean oceanic advection and anomalous surface heating/cooling through surface heat flux (Fs) and Ekman advection (Fek).

The layout of the paper is as follows: observations of the variability in the ACC are described in Section 3.2. In Section 3.3, a simple model of SST propagating in the mixed layer is forced with observed heat fluxes (Fs+Fek), in order to identify which components of the heat fluxes are important to explain the observed SST variability. The relevance of ENSO and SAM in driving those heat fluxes is presented in Section 3.4. In Section 3.5, the physical mechanism is related to the resonant advection mechanism of Saravanan and McWilliams [1998], and the spectral response of the ocean to ENSO and SAM forcing is examined. Ocean-atmosphere coupling is discussed in Section 3.6, and the main results are summarized in Section 3.7.

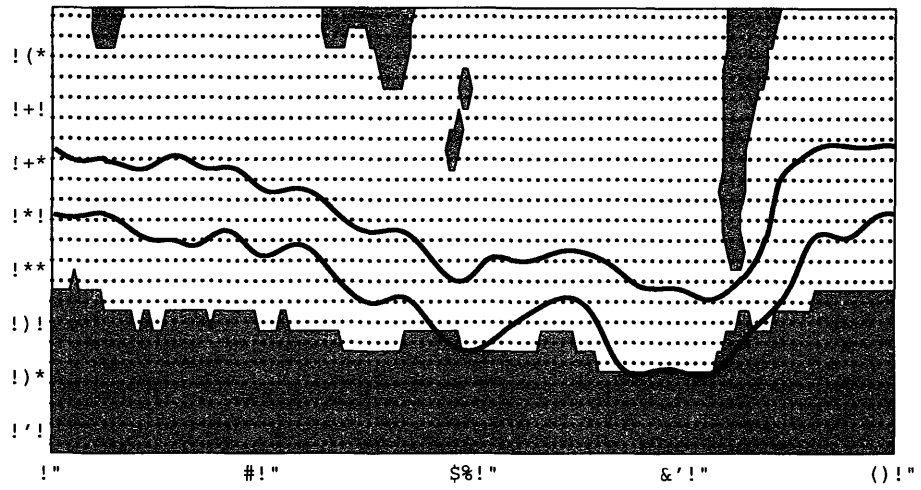

Figure 3-1: Two geostrophic streamlines encircling the globe, delimiting the region of the ACC, plotted over the data grid points (from NCEP-NCAR Reanalysis); for clarity only half the points are shown in the zonal direction. Shaded areas represent land masses and sea ice.

3.2 Observed variability in the ACC

3.2.1 Methodology

We use the dataset from the National Centers for Environmental Prediction and the National Center for Atmospheric Research (NCEP-NCAR) Reanalysis [Kalnay et al., 1996] over the period 1980-2004. This period is chosen because it incorporates satellite based SST estimates: from 1982 onward, the Reanalysis employs Reynolds SST (analyzed data from the Advanced Very High Resolution Radiometer, AVHRR). Prior to the 1980s, SST observations were limited to ship and buoy measurements. Other fields used in this study, such as heat fluxes, are not directly constrained by observations and thus are subject to larger inaccuracies; for the more recent period, however, the modeled variables show similar statistics to that of the ECMWF Reanalysis [Sterl, 2004], suggesting reasonable reliability.

Surface data is provided on a grid with a resolution of approximately 2^ox2^o; here we consider monthly averages. All time series are linearly detrended, but otherwise not

filtered. The variability is computed by removing the mean seasonal cycle, calculated at every grid point. Departures from the seasonal cycle are defined as "anomalies".

The variability is analyzed along the path of the ACC. For this purpose, we estimate the position of the current using sea surface height data from the TOPEX-Poseidon altimeter. Following Karsten and Marshall [2002], the 4-year averaged dynamic sea surface height is compared with a reference geoid to evaluate the geostrophic streamfunction (Ψ):

$$\Psi = \frac{gh}{f} \tag{3.1}$$

where f is the Coriolis parameter, g is the gravitational constant, and h is the sea surface height. The geostrophic flow is given by the gradient of Ψ:

$$(u_g, v_g) = \hat{z} \times \nabla\Psi \tag{3.2}$$

where $\hat{z}$ is a unit vector in the vertical direction.

The mean path of the ACC is defined here as the region bounded by the two circumpolar streamlines that flow around the globe without intercepting land (Figure 3-1). Observations are averaged over the width of the current. This procedure is justified by the fact that the dominant structures of anomalous SST and surface heat fluxes, obtained from empirical orthogonal function (EOF) analysis, exhibit little variations across the ACC (not shown). Data falling on sea ice is excluded. Land masses and sea ice are shaded on Figure 3-1.

3.2.2 Along-stream variability of SST

First we examine the distribution of SST anomalies in time and space. In Figure 3-2, the variance of surface temperature anomalies along the path of the current is presented as a function of calendar month. Monthly SST anomalies have typical magnitudes of 1K; the interannual signal is thus not negligible compared to the seasonal cycle, which has a total amplitude of approximately 3K (not shown). Most of the

variability occurs in the central Pacific, between 200E and 300E. At those latitudes the current flows closest to sea ice (Figure 3-1). It also coincides with the end of the storm track [Nakamura and Shimpo, 2004], associated with enhanced wind variability. For these two reasons, the heat fluxes are expected to be more variable in this region, driving anomalous SST.

Seasonal variations are evident in Figure 3-2; the variance is strongest during the austral summer months (January through March). This time dependence is thought to result from variations in mixed layer depth: unlike in the Northern Hemisphere, atmospheric forcing in the Southern Hemisphere exhibits little seasonal variation; the amplitude of anomalous heat fluxes at the sea surface being constant throughout the year, the resulting SST anomalies are less important when the mixed layer is deep, which happens in the winter when mode waters are forming [Levitus and Boyer, 1994].

The dominance of SST variability in the Pacific was also observed by Cai and Baines [2001] , who relate it to the location of the Pacific-South America pattern, a surface pressure anomaly. Yuan and Martinson [2000] notice that sea ice variability is strongest in the Pacific.

3.2.3 Along-stream covariability of SST and SLP

The SST variability is now related to sea level pressure (SLP) fluctuations through a maximum covariance analysis (mca) of streamline-averaged anomalies. This technique also called singular value decomposition is used to identify the orthogonal modes of variability in two covarying fields [Bretherton et al., 1992]. It is performed here on monthly data; for the 24 year period considered, the analyzed time series have 288 data points.

Figure 3-3 shows the patterns and their associated time series for the two leading modes of covariability, accounting for 63% and 21% of the squared covariance, respectively. The first mode accounts for 20% of the SST variance, and 24% of the SLP

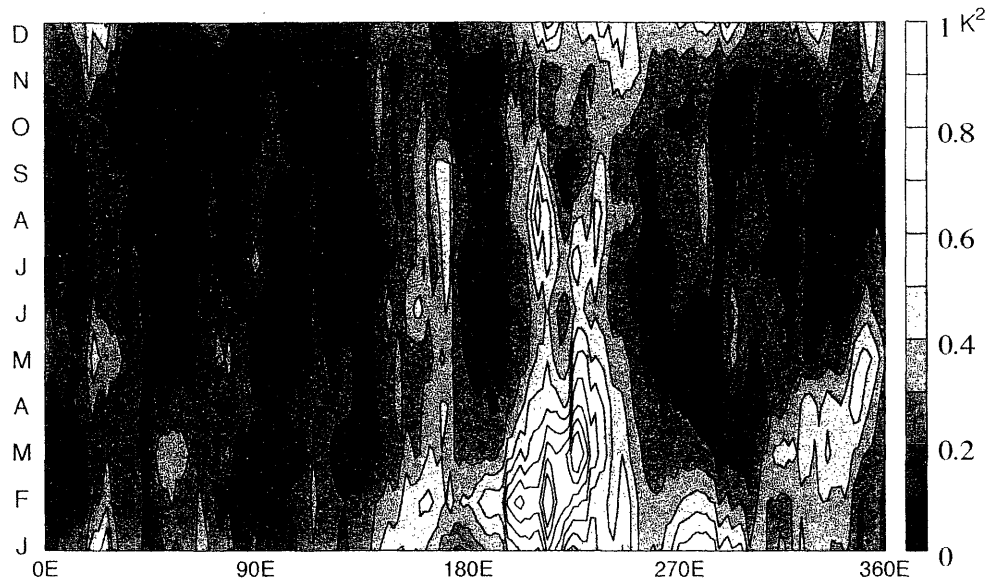

Figure 3-2: Variance of SST anomalies along the ACC (x-axis is longitude), as a function of calendar month. The variability is greatest in the Pacific sector (200E to 300E); it is enhanced during the Austral summer when the mixed layer is shallowest.

variance (as a reference the first EOFs of streamline-averaged SST and SLP explain 22% and 27% of their respective variance). The time series associated with the first mca mode will be subsequently referred to as SST-mca and SLP-mca. The second mode, which has weaker amplitude, accounts for 11% and 21% of SST and SLP variance, respectively. These spatial patterns are essentially localized in the Pacific basin, both for temperature and pressure anomalies.

For both modes, the SLP maximum is slightly to the east of the SST maximum; in the Pacific they are separated by roughly 45 degrees in longitude. A simple explanation is that the advection of air around the high pressure center is reinforced by advection of air around the low pressure anomaly at 200E; both drive ocean-atmosphere exchanges of heat around 250E, which is the location of the SST-mca maximum. The spatial configuration supports the idea that heat fluxes induced by anomalous low-level atmospheric circulation is involved in the generation of SST anomalies. Similar analysis with covarying SST and meridional winds show that the position of maximum

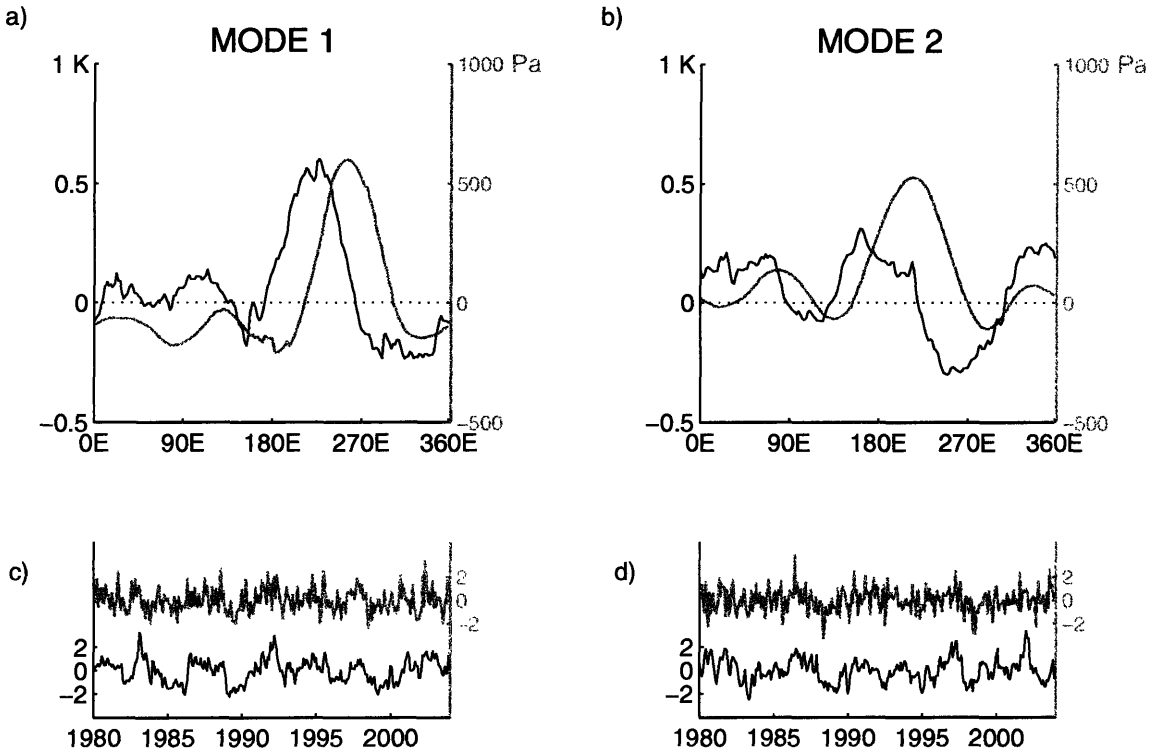

Figure 3-3: First and second modes of variability of SST (black) and SLP (gray) showing the maximum covariance along the ACC. The spatial patterns for mode 1 and 2 are presented in a) and b) respectively. Mode 2 is upstream of mode 1 and has weaker amplitude. The amplitude shown corresponds to a typical change in SST (in K) or SLP (in Pa) for a 1 standard deviation of the associated time series. The normalized time series associated with the spatial patterns are presented in c) and d).

winds does indeed coincide with the SST maximum (not shown).

We also find that the covariance between SST-mca and SLP-mca is a maximum when the pressure signal leads by one month. This time lag is consistent with the scenario of a passive response of the ocean to atmospheric forcing, the ocean taking a few weeks to adjust to the change in heat fluxes. This result suggests that SST is driven by the SLP mode, and not vice-versa. Based on these observations, we claim that SST variability in the ACC is forced by a low-level atmospheric pattern localized in the Pacific.

3.2.4 Propagating modes of SST variability

From the mca, we find that the SLP signal is essentially standing; its autocorrelation has an e-folding timescale of only 1 month. For this reason it is hard to obtain evidence for the propagation of SLP anomalies, and indeed our analysis revealed no significant indication of propagation. On the other hand, we find that SST modes 1 and 2 are not independent, but correspond to a single propagating mode. The second mode leads the first by approximately 1 year (correlation not shown here). The propagation of the SST anomalies is highlighted by performing a lagged correlation of the SST-mca mode with the time series of observed SST at every longitude, along the path of the ACC (Figure 3-4). On the figure, shaded regions indicate where correlations are significant at the 95% level; we take 3 months as a null hypothesis for midlatitude SST decorrelation time, and thus consider $Nt/3$ degrees of freedom for a time series containing Nt data points.

At zero lag, following the horizontal dashed line, the pattern of Figure 3-3 is retrieved: the amplitude of the signal is greatest in the central Pacific. As the lag increases, the peak correlation moves to the right, indicating that the pattern of anomalous temperature has moved eastward. From the slope of the correlation bands on Figure 3-4 we infer the propagation speed to be 8 cm/s. This value coincides with the mean geostrophic velocity of the ACC, estimated from the geostrophic streamfunction defined in (3.2). The meridional gradient of Ψ calculated from the two circumpolar streamlines shown in Figure 3-1, gives the geostrophic velocity averaged across the current; the average of this velocity along the current is 8 cm/s. This suggests that the SST anomalies are passively advected by the current.

Significant correlations appear to be centered around the Pacific basin and limited to ± 2 years lag. The fact that higher correlations are found downstream (positive lag) than upstream of the Pacific suggests that anomalies originate from that region and are then advected away. In addition, a superposition of wavenumbers 1 and 2 appear to dominate the spatial structure. In the next section, we show that these

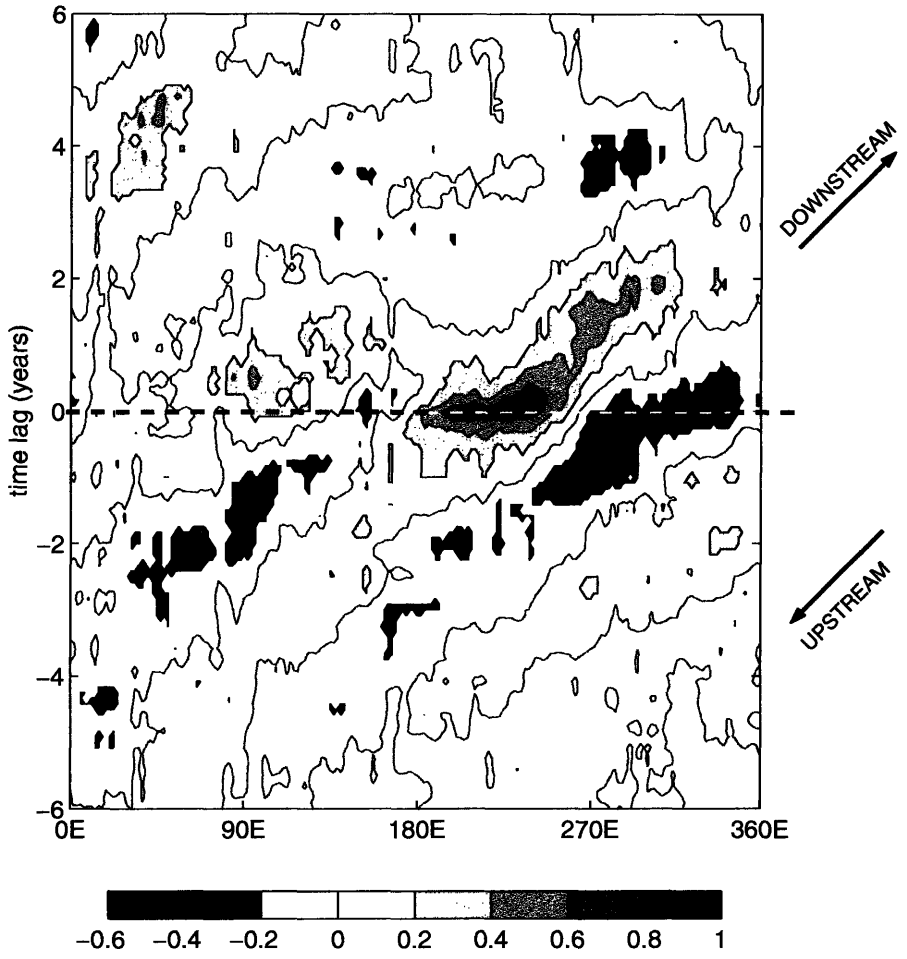

Figure 3-4: Lagged correlation of observed SST with the first SST-mca mode (from Figure 3-3). At zero lag, following the horizontal dashed line, the pattern of Figure 3-3a is retrieved. Lighter shades of gray indicate positive correlations and darker shades, negative correlations; only values that are significant at the 95% level are shown. The location of the maximum correlation ($\sim$ 210E at zero lag) is displaced to the right as lag increases, indicating eastward propagation of the signal. The speed of propagation is estimated from the figure to be 8 cm/s, which coincides with the mean advection velocity of the ACC. If they persisted, anomalies propagating at that speed would encircle the globe in approximately 10 years.

characteristics can be understood as a response of the mixed layer to mean oceanic advection and anomalies in surface heat flux and Ekman advection. In sections 4 and 5 we will argue that the wavenumbers 1 and 2 reflect SAM and ENSO forcing.

3.3 A diagnostic model of SST anomaly

In order to study the extent to which the observed SST variability can be explained by observed heat fluxes, we employ a 1-dimensional model of SST propagating in the ACC. It is forced by observed heat fluxes.

3.3.1 Heat flux variability

Turbulent surface heat fluxes occur via exchange of latent and sensible heat at the air-sea interface. The sensible heat flux and latent heat flux are obtained from the Reanalysis, and summed. As a preliminary diagnostic, we calculated the surface heat fluxes from the linearized bulk formulae, and found the calculated values to be very similar to those of the Reanalysis. The two components of the linearized bulk formulas contributing to heat flux variability have similar magnitude; one is due to anomalous wind and the other is due to anomalous temperature and moisture at the sea surface. Together the two components add up to surface anomalous heat fluxes with a standard deviation of 12 to 28 W/m^2, depending on the position along the current.

In addition, we also consider heat fluxes resulting from anomalous Ekman advection in the upper ocean, acting on mean temperature gradients (especially in the meridional direction). We estimate Ekman fluxes from wind stress anomalies from the Reanalysis:

$$F'_{ek} = \rho c_P \left(\tilde{\mathbf{u}}'_{ek} \cdot \nabla \overline{T} \right) \tag{3.3}$$

where $\tilde{\mathbf{u}}'_{ek} = -\frac{1}{\rho f} \left(\hat{k} \times \tilde{\tau}' \right)$ is the anomalous Ekman transport in the ocean; $\vec{\tau}'$ is the wind stress anomaly and $\nabla \overline{T}$ is the seasonally varying SST gradient; f is the Coriolis parameter; ρ and c_p are the density and heat capacity of seawater, respectively.

3.3.2 Description of the model

The model is set-up in a similar fashion as the stochastic model with ocean advection of Saravanan and McWilliams [1998], but in our case the random forcing is replaced by the observed heat fluxes described above. Here we consider oceanic advection along the x-axis, which we choose to be parallel to the path of the ACC defined in Section 3.2. Heat flux data is averaged meridionally over the width of the current.

The temperature equation in the mixed layer, linearized around the mean seasonal cycle, is:

$$\frac{\partial}{\partial t}T' + \bar{u}\frac{\partial}{\partial x}T' = \frac{1}{\rho c_P h}\left[-\alpha T' + (F'_{ek} + F'_s)\right] \tag{3.4}$$

For the advective velocity, we take the mean geostrophic velocity of the ACC, $\bar{u} =$ 8 cm/s. This value was determined as the temporal and spatial average of the along ACC velocity calculated from TOPEX-Poseidon data (section 3.2.1). The depth of the mixed layer, h, is assumed constant with a value of 100 m. From Levitus climatology, we know that h is spatially inhomogeneous, and that it varies seasonally from about 50 m in the austral summer, to more than 500 m in the winter in convective locations; however we found that taking a constant value does not qualitatively affect the result of the simulation. Similarly, choosing a different value for h (still constant) affects the magnitude but not the patterns of simulated SST anomalies. By considering uniform velocity and uniform depth, we ensure that the transport is constant along the current, assuming that the bounding streamlines separation does not vary.

The damping parameter, α, represents the terms that are not explicitly included in (3.4): vertical entrainment and horizontal diffusivity. We choose a value of $\alpha = 20$ W/m^2/K for this tunable parameter, which corresponds to a damping timescale of 9 months for a mixed layer depth of 100 m. This value gives the most realistic persistence of SST anomalies. The temperature equation is integrated numerically; it is discretized using a forward in time, upwind in space scheme. This scheme leads to numerical damping, but we find it to be negligible compared to the timescale of

damping to the atmosphere (α^{-1}). Initially, the anomalous SST field is set to observed values for January 1980.

3.3.3 Simulated SST variability

The simulated SST is presented in Figure 3-5 as a function of longitude and time. It was obtained by introducing the observed heat flux and Ekman advection of heat into (3.4). The high-frequencies of the forcing are filtered out by the model; this is explained by the slow oceanic response (causing the reddening of the SST spectra in Hasselmann's theory). For comparison, the observed SST field is also presented in Figure 3-5 as a function of longitude and time. A visual examination of the two diagrams reveals that the model captures the propagation and timing of the observed basin-scale SST. Eastward propagation in the modeled field occurs at the prescribed velocity (8 cm/s). The agreement between simulated and observed fields is particularly good in the Pacific and Western Atlantic.

A quantitative comparison of the simulation with the observations is obtained by cross-correlating their respective EOFs. The first mode of variability of the observed SST is strongly peaked around 230E (in the Pacific) and accounts for 22% of the variance. For the simulated SST, the first EOF, accounting for 32% of the variance, has a different spatial pattern; the peak centered in the Pacific is retrieved in the second EOF, which accounts for 27% of the variance. The correlation between EOF1 of the observations and EOF2 of the simulation is $\rho = 0.48$.

Differences between the two fields can be explained by the simplicity of the model, which does not represent uncertainties in the forcing, eddy turbulence, vertical entrainment and other ocean dynamics. These processes are responsible for spatial and temporal small-scale variability, not captured by the model.

Figure 3-6 shows that both the simulated and observed fields exhibit more variability in the Pacific basin. Since the model's mixed layer depth is constant in space, this enhanced variability must arise from spatial inhomogeneity of the surface forc-

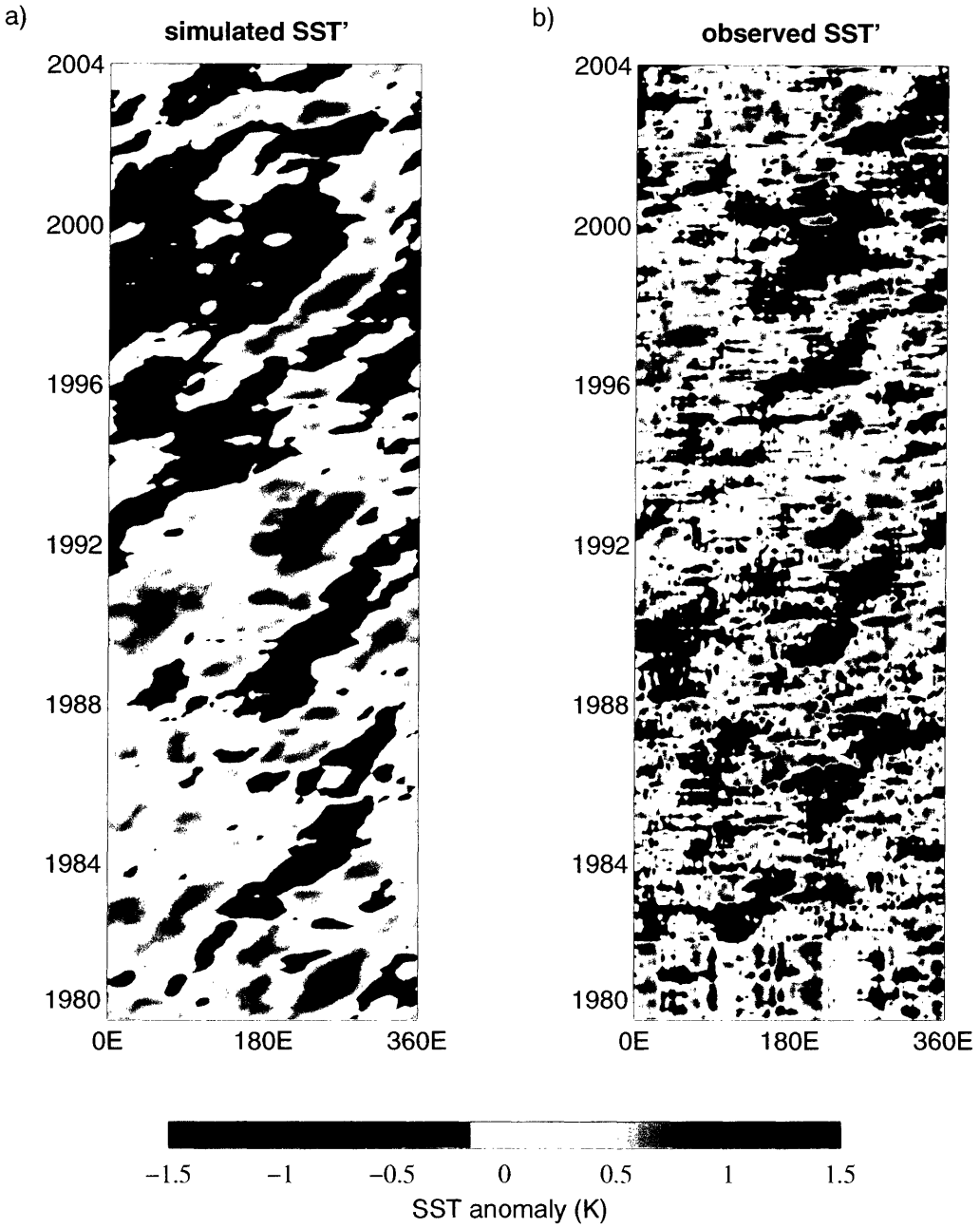

Figure 3-5: Time-longitude diagrams of a) the SST simulated from the heat fluxes, estimated from the Reanalysis and introduced in Equation 3.4; b) observed SST from the Reanalysis. The simulated field captures the propagation and timing of the observations.

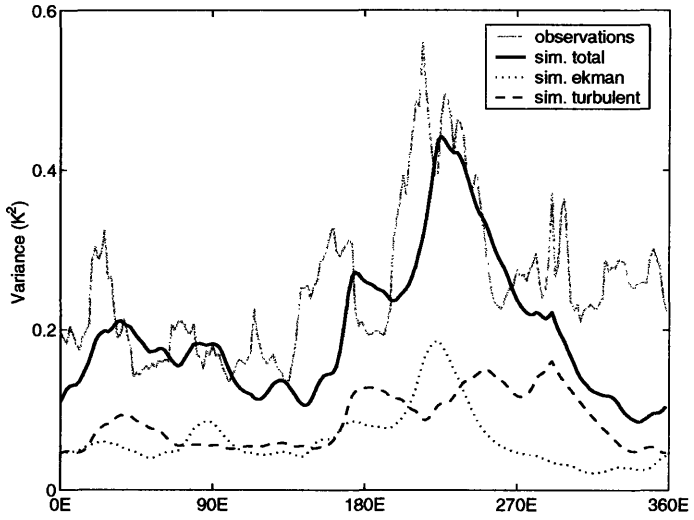

Figure 3-6: Variance of SST as a function of longitude (along the path of the SST). Gray line: observations; dotted line: simulated from Ekman heat fluxes; dashed line: simulated from surface heat fluxes; black solid line: simulated from Ekman + surface heat fluxes.

ing. Inspection of the heat fluxes does indeed reveal that their variance is greater in the Pacific than in other basins, consistent with the analysis of Section 3.2.3. The amplitude of the simulated variance is sensitive to the choice of α; stronger damping induces weaker variability. The value $\alpha = 20$ W/m^2/K leads to simulated SST variance which is similar to the observations.

The relative importance of the surface heat fluxes versus Ekman advection can be assessed by performing simulations with each component separately. SST driven from Ekman fluxes alone, as well as SST driven from surface fluxes alone, have more variability in the Pacific (Figure 3-6). In both cases, SST variance is considerably less than when the total heat flux field is used. This indicates that Ekman and surface fluxes reinforce rather than cancel one another. The magnitude and variance of simulated SST anomalies is similar in both cases, suggesting that Ekman and turbulent fluxes are each responsible for approximately 50% of the SST variability.

3.4 Mechanisms of external forcing

3.4.1 SAM and ENSO

Since we have demonstrated in section 3.3 that Fs+Fek is the main driver of SST variability along the ACC, we now investigate what physical mechanisms drive the observed heat fluxes. From the maximum covariance analysis presented in Section 2, a coupled system seems unlikely, since the SLP variability tends to lead in time the SST variability. The other possible scenario is one in which the ocean reacts passively to the forcing. In this case one can ask: what are the primary sources of atmospheric variability?

We examine two sources of atmospheric forcing: ENSO and SAM. ENSO is a coupled ocean-atmosphere phenomenon originating in the tropics. It is thought to reach the ACC via atmospheric teleconnections: possible mechanisms include propagation of the signal by atmospheric Rossby waves [Karoly, 1989], and changes in the Ferrell cell [Liu et al., 2002]. We use Niño3 as an index for ENSO-related variability [Cane et al., 1986]; it is calculated from the SST averaged between 5S and 5N, from 150W to 90W. Most of its energy is in the 3 to 7 years period band [Wunsch, 1999].

SAM is an important source of monthly and interannual variability in the atmosphere, also referred to as the Antarctic Oscillation (AAO). In its positive phase it is characterized by a contraction of the polar vortex [Thompson and Wallace, 2000], which is expressed at the sea surface by an enhancement of the westerlies in the region of the ACC. A measure of the strength of SAM is given by the "SAM index", calculated from the principal component of the first mode of variability of the 850 hPa field between 20S and 90S [Thompson and Wallace, 2000]. On timescales of a month or longer, it has a white spectrum.

The two indices are found to be strongly correlated with the SST signal. The SAM and Niño3 indices are plotted in Figure 3-7, along with the time series of SST-mca. One observes a close correspondence between all time series, with the lagged

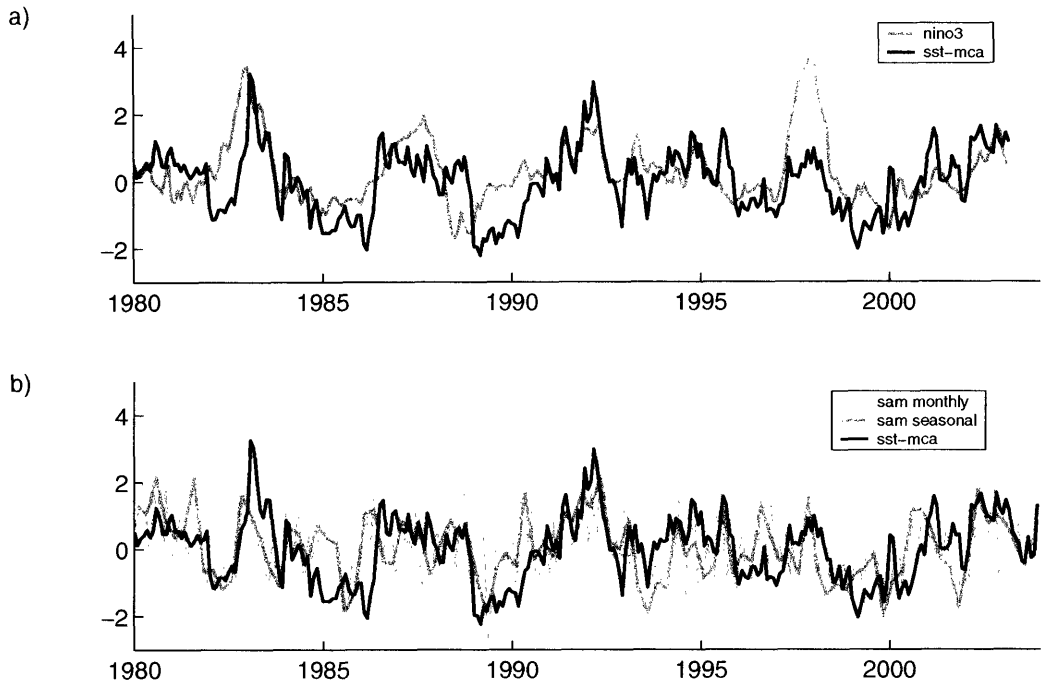

Figure 3-7: Time series of SST-mca, black line, in both panels. a) Niño3 (gray line) and b) SAM index (thin gray: monthly data, thick gray: seasonal averages). Each index is normalized.

cross-correlations peaking when SAM and ENSO lead in time; this is consistent with an atmospheric driving of SST variability. It is found that the correlation with Niño3 has a coefficient of 0.53, when the temperature lags by 1 month. The correlation with SAM has a coefficient of -0.38, when the temperature lags by 1 month; the correlation is -0.47 when seasonal averages are considered. Together ENSO and SAM explain approximately 45% of the leading mode of SST covarying with the atmosphere (the fraction of variance explained is given by the square of the correlation coefficient). In such estimates, we have assumed that the annular mode is independent of ENSO. This hypothesis seems reasonable as they have very different dynamics, and we were unable to show any dependence of one index upon the other.

The SLP-mca mode is also found to be associated with SAM and ENSO. The correlation coefficient between SLP-mca and ENSO is 0.33, and with SAM it is -0.58

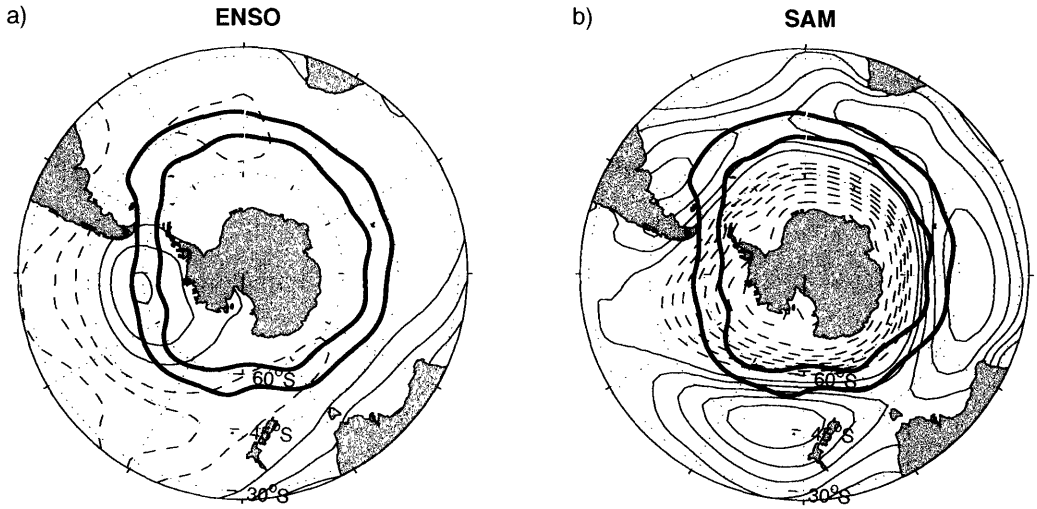

Figure 3-8: Correlation of SLP with a) Niño3 index and b) SAM index; solid (dashed) contours indicate positive (negative) correlations. The contour interval is 0.1; the zero contour is not drawn. Thick black lines show the mean position of the ACC as defined in Section 3.2. In the ACC band, both signal exhibit a strong pressure anomaly in the South-East Pacific.

(0.43 and -0.65 for seasonal averages).

ENSO and SAM are both found to affect the low-level atmospheric circulation in the South Pacific. The patterns can be seen in Figure 3-8, showing the correlations of monthly SLP anomalies (from the Reanalysis) with the Niño3 index and the SAM index. In both cases SLP variations are found along the path of the ACC, allowing for possible interactions between ocean dynamics and atmospheric forcing pattern. The geostrophic flow induced by the anomalous pressure is expected to drive SST anomalies by advecting cold / warm air across the temperature front of the ACC.

The surface pressure pattern associated with SAM has an annular shape, but it is not exactly zonally symmetric: it extends to lower latitudes in the Pacific sector (Figure 3-8). In that same region, the ACC streamlines bend toward the continent as the current flows through Drake Passage. As a result, the ACC intercepts a zone of strong pressure gradients, which will affect the heat fluxes in the ocean. In contrast, the ENSO teleconnection is more localized to the eastern Pacific sector. El Niño

events are associated with a high pressure center (low pressure during La Niña).

3.4.2 SAM and ENSO heat flux patterns

Here we analyze the spatial patterns associated with heat fluxes induced by ENSO and SAM, in order to illuminate their role in the generation of SST anomalies. This is done by regressing the heat fluxes onto the SAM index and Niño3 index. The resulting spatial patterns are shown in Figure 3-9. These patterns correspond to the heat fluxes occurring during an anomalous index with an amplitude of 1 standard deviation (1σ). The spatial pattern multiplied by the index time series, gives the actual observed heat fluxes.

As evidenced in Figure 3-9, the heat flux variability induced by ENSO occurs principally in the Pacific sector, which is consistent with the location of the ENSO-driven low-level circulation pattern (Figure 3-8). In an El Niño year, anomalous meridional advection along the path of the ACC leads to surface warming in the central Pacific, and cooling in the western Pacific and downstream of Drake Passage. At the same time, Ekman advection in the ocean induces warming in the Pacific sector. The signs of the fluxes are reversed during a La Niña episode. Surface heat fluxes and Ekman heat fluxes interact constructively in the central Pacific; this region coincides with the location where SST variance is observed to be maximum.

SAM displays a similar pattern of surface heat fluxes, with a tripole structure in the Pacific sector. This is superimposed on a zonally symmetric signal associated with Ekman heat fluxes. The latter is efficient in driving cooling of the upper ocean in the ACC band during a positive phase of the annular mode. Once again, the two patterns of simultaneous variability enhance each other in the central Pacific.

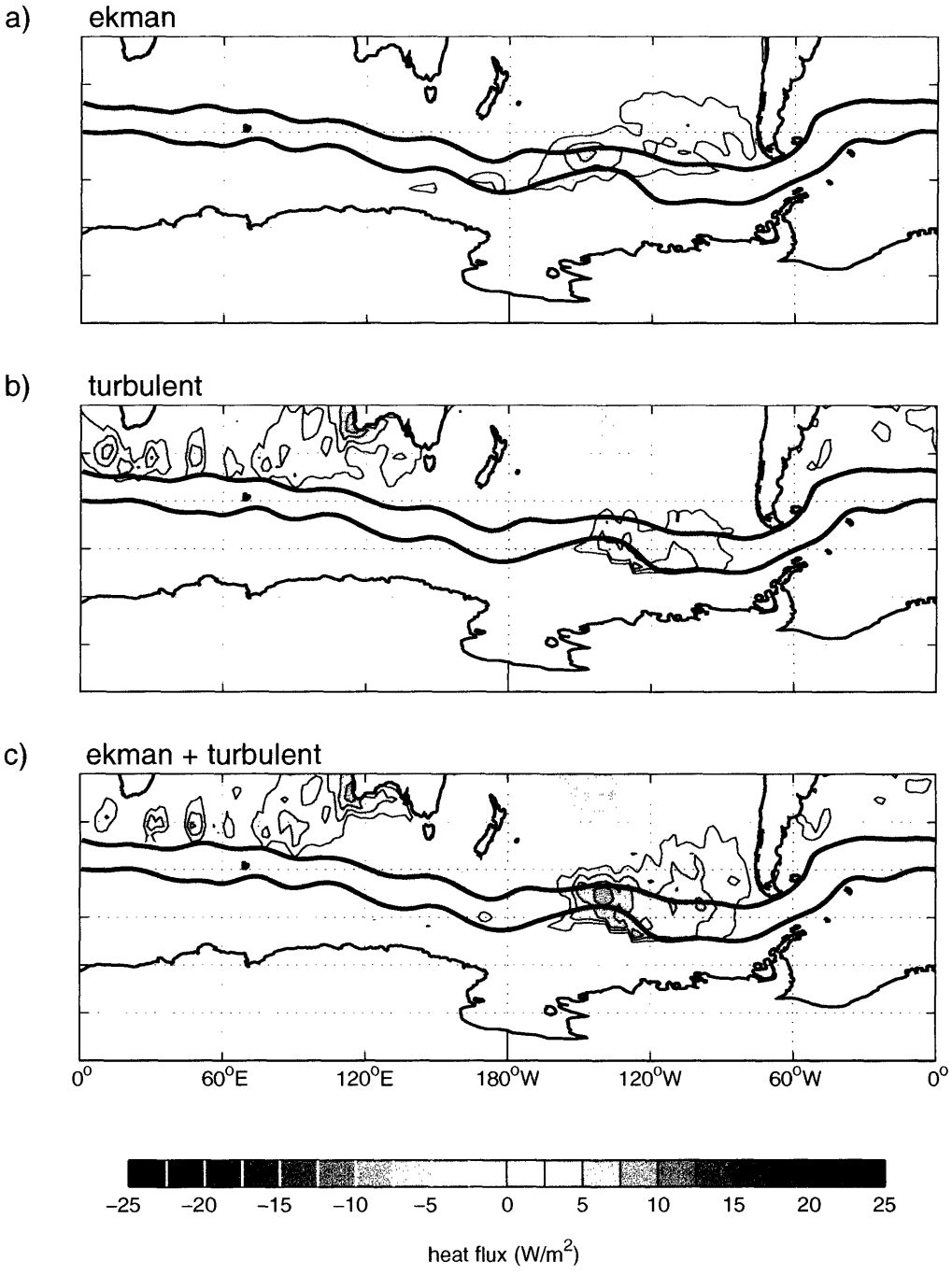

Figure 3-9: Regression of monthly heat fluxes anomalies (in W /m^2) onto Niño3 and the SAM index. a) and d) show the surface turbulent heat fluxes (sensible + latent); b) and e) show the Ekman heat fluxes; c) and f) show the sum of the two components (surface + Ekman). Heat fluxes are defined as positive when into the ocean. Continued on the next page.

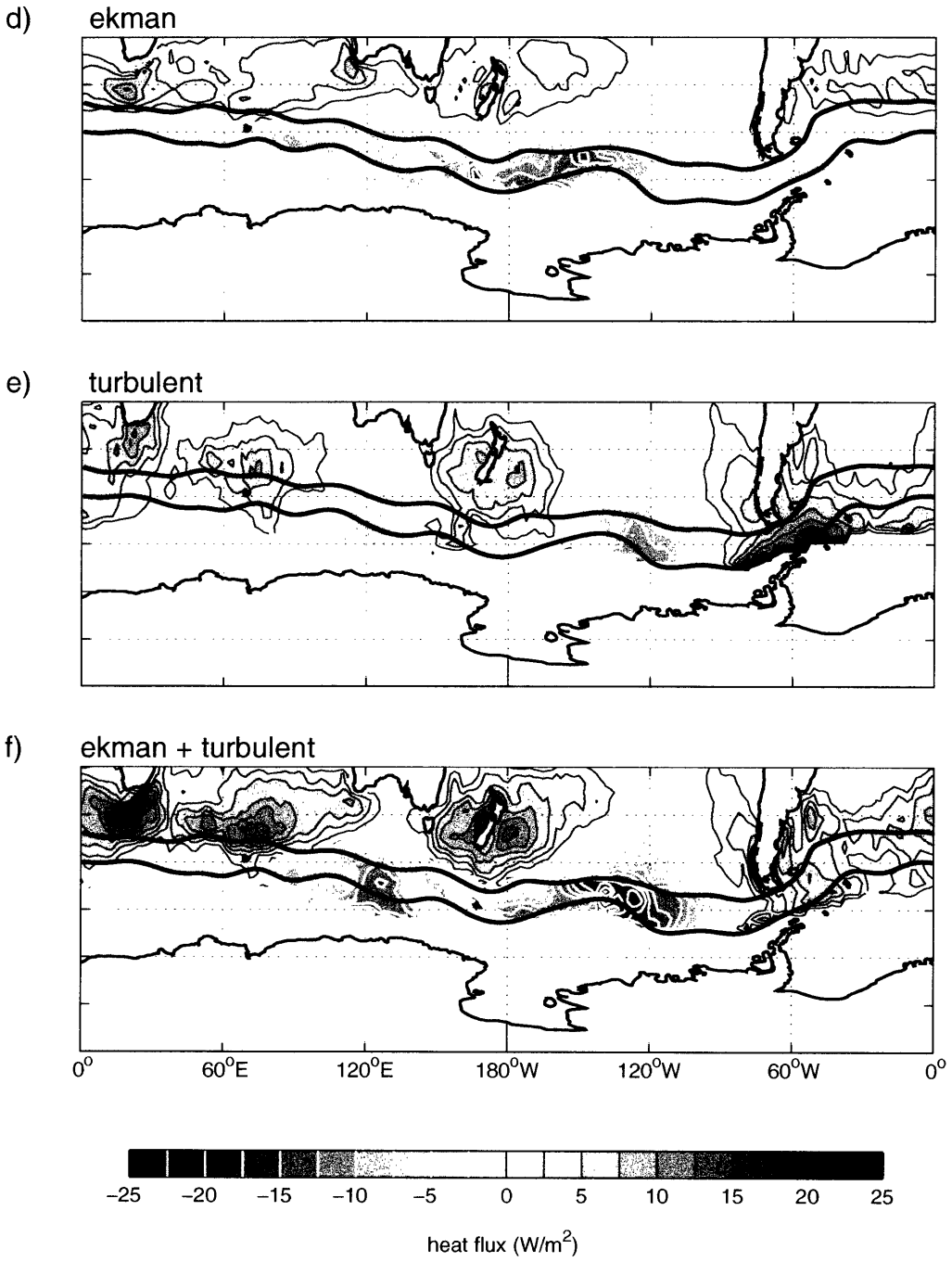

Figure 3-9 (continued): See caption on previous page.

3.4.3 SAM and ENSO impact on SST

We now assess the relative importance of the heat fluxes driven by ENSO and SAM, in explaining the observed SST. The heat fluxes regressed on ENSO and SAM are introduced in the flux model of Section 3.3. We construct a matrix of the forcing: spatial patterns, seasonally varying, multiplied by the index time series (SAM-index and Niño3). Note that here, the spatial patterns are calculated for each of the four seasons, to account for the fact that heat fluxes are different in the summer than in the winter (Figure 3-9 showed the annual mean patterns).

Simulated SST are presented in Figure 3-10. The simulation with both fields is simply the sum of the simulation with ENSO and the simulation with SAM, since the model is linear. The simulation with ENSO reproduces the strong events of 1982-83 and 1997-98. However, it seems as though most of the higher frequency variability is induced by SAM. Both sources of external forcing are associated with SST variability in the Pacific basin.

We can test the relevance of the simulated field to the observations, by comparing their first EOF. The correlations between the time series are: $\rho = 0.57$ for the ENSO-only simulation, $\rho = 0.63$ for the SAM-only simulation, and $\rho = 0.70$ for the simulation with both fields. The best simulations are obtained with both SAM and ENSO induced heat fluxes, which means that they are both important in creating the observed SST variability.

In all three cases, the correlation is higher than that obtained for the simulation with the total heat fluxes (Section 3.3.3). This implies that the mode of variability along the ACC which has a spatial pattern centered in the Pacific sector is better reproduced with ENSO and/or SAM induced forcing. It suggests that other components of the forcing reduce the quality of the simulation. These results support our hypothesis, that SAM and ENSO are two drivers of SST variability along the ACC (Section 3.4.1) and that their effect is concentrated in the Pacific basin (Figure 3-8).

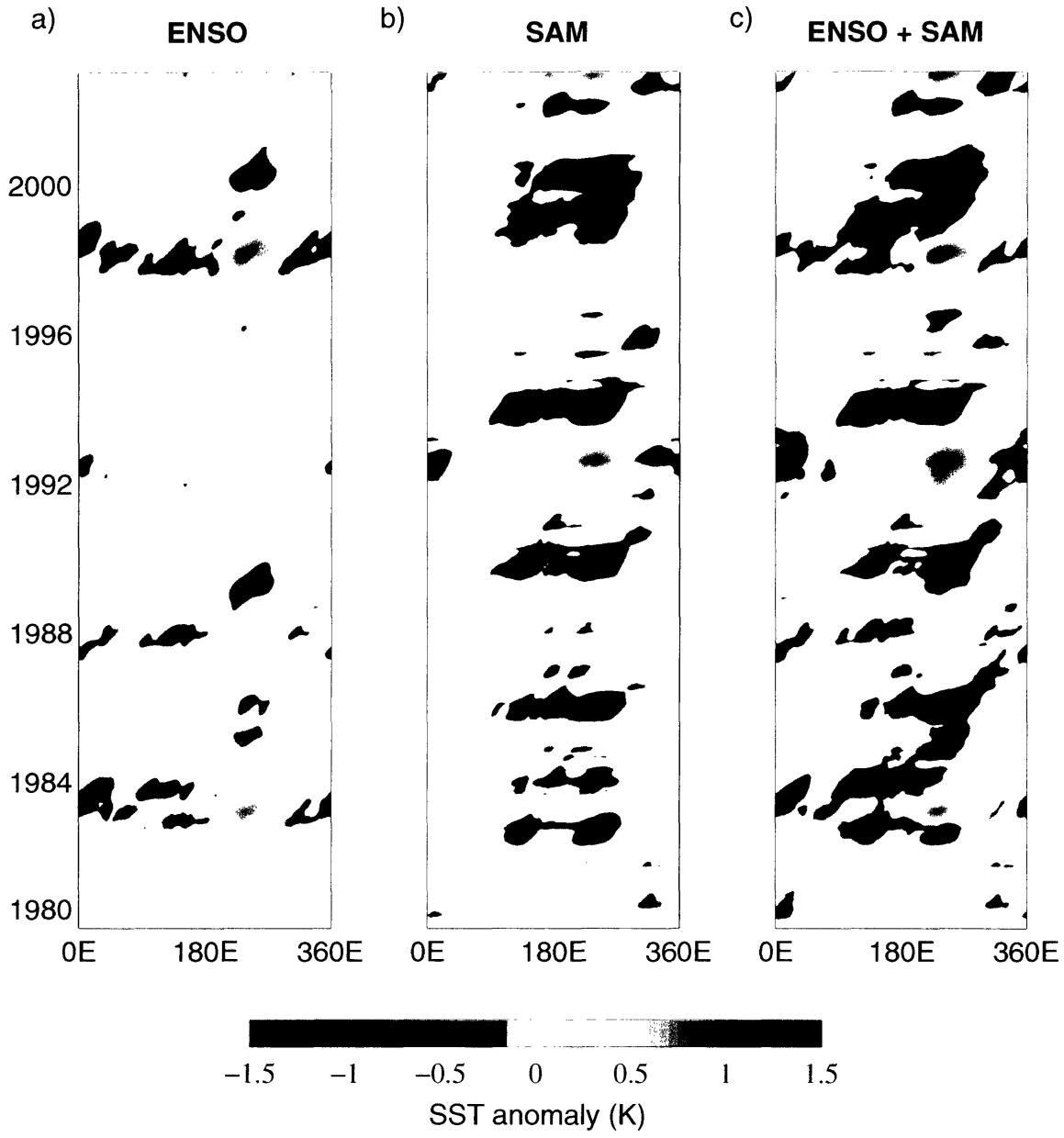

Figure 3-10: Time-longitude diagrams, showing the SST simulated from the heat fluxes regressed on a) Niño3, b) SAM, c) Niño3 + SAM.

3.5 Spectral response of SST to stochastic forcing

Having identified SAM and ENSO as the dominant sources of atmospheric forcing, we now relate their impact on SST to the advective resonance mechanism proposed by Saravanan and McWilliams [1998], which can be extended in periodic domains such as the ACC region [Weisse et al. 1999; Scott 2003]. We begin by reviewing some important concepts of the mechanism; a more complete discussion is found in Weisse et al. [1999].

3.5.1 Resonant advection mechanism

The ocean's response to stochastic forcing, in the presence of a mean oceanic flow, depends on the advection speed and the timescale for the dissipation of SST anomalies. In the model of Section 3.3, we introduced a damping term, α; that term did not include the dissipation of temperature anomalies via air-sea heat fluxes, which was already accounted for in the F'_s term of (3.4) (F'_s includes both the effects of atmospheric forcing and oceanic feedbacks). The total damping, including air-sea heat fluxes, will be represented by the symbol λ; it is equivalent to the λ_{eff} of Equation 9 in Saravanan and McWilliams [1998].

The temperature equation (3.4) can be rewritten (dropping the primes)

$$\frac{\partial}{\partial t}T + \bar{u}\frac{\partial}{\partial x}T = -\lambda T + F \tag{3.5}$$

where F represents the surface and Ekman heat flux forcing, F'_{ek} and F'_s in (3.4); the factor $\rho c_P h$ is absorbed in the variables λ and F.

From (3.5) we can relate the SST spectrum (E_T) to the spectrum of the forcing (E_F),

$$E_T(\omega, k) = \frac{E_F(\omega, k)}{(\omega - k\bar{u})^2 + \lambda^2} \tag{3.6}$$

where the (k, ω) spectrum E_X is defined as $E_X =< \hat{X}\hat{X}^* >$; $\bar{u}$ is the mean advective

velocity, k is the spatial wavenumber, ω is the angular frequency and brackets denote ensemble average.

If the forcing is a white noise, then $E_F = E_F(k)$; it does not depend on the frequency. In that case, (3.6) predicts a peak in the ocean $k\omega$ spectrum at the frequency $\omega = k\bar{u}$. If the forcing has a dominant wavenumber k_0, the peak is located at $\omega = k_0\bar{u}$, corresponding to an advective timescale of

$$T_{adv} = \frac{2\pi}{k_0\bar{u}} \tag{3.7}$$

This timescale appears as the preferred period of oceanic variability, even though the atmospheric forcing is white. It corresponds to the Fourier mode for which the reversal of the polarity of the forcing (half a period) takes the same time as the advection of SST anomalies between two poles of the sinusoidal forcing pattern (half a wavelength); anomalies created under one pole thus get amplified under the next pole. This results in SST anomalies that are long-lived, propagate at the speed of the ocean current and have a preferred timescale in the SST spectrum. All other frequencies (Fourier modes) interact destructively with the ocean.

In a periodic domain such as the Southern Ocean, the resonance mechanism would lead to infinite SST response if there were no damping or friction; the original scenario of anomalies propagating in a bounded domain [Saravanan and McWilliams, 1998] is a "finite resonance", since the SST response would remain finite even if the damping vanished.

In the ocean, $\bar{u}$ is rather small, typically a few centimeters per second. k_0 is also small when large-scale forcing is considered. Thus T_{adv} is large, which means that the oceanic variability induced by stochastic forcing has a low frequency, ranging from interannual to decadal variability.

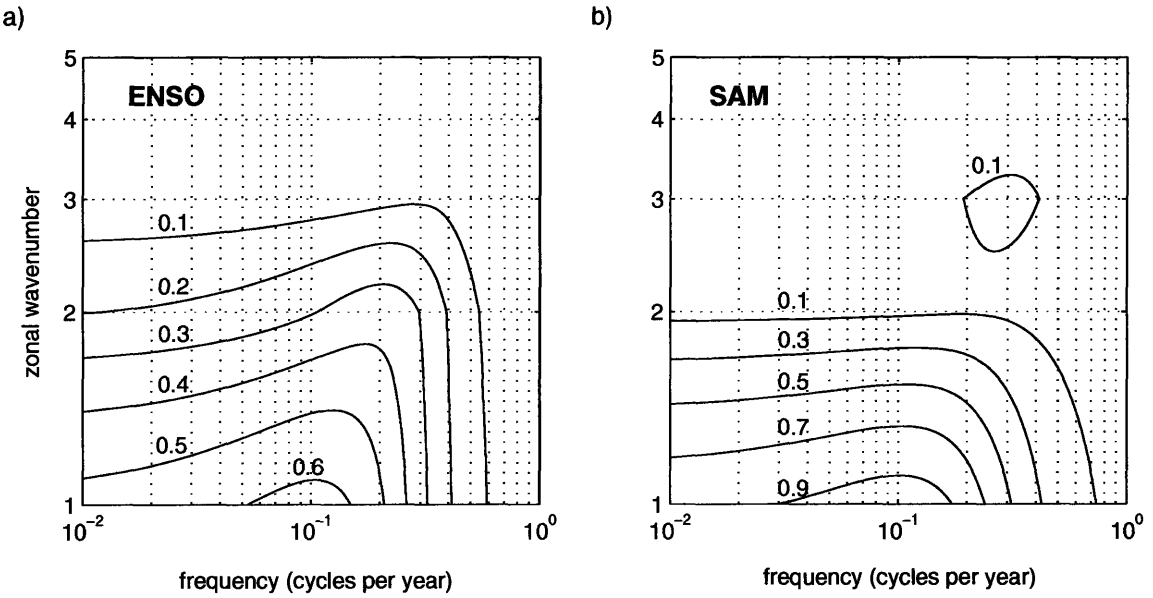

Figure 3-11: Wavenumber-frequency spectrum for SST, as predicted from Equation 3.4, assuming a white-noise forcing with the spatial pattern of a) the heat fluxes regressed on ENSO, as shown in Figure 3-9c; and b) the heat fluxes regressed on SAM, as shown in Figure 3-9f. Both spectra are normalized by the peak value of the SST spectrum in b). The ocean response is expected to be at low wavenumbers, with a dominant period of 10 years. Note that the spectrum is continuous in ω but discrete in k. The spectra were calculated with $\lambda = \alpha \simeq (9 \text{ months})^{-1}$.

3.5.2 Spectral response to ENSO and SAM

To relate SAM and ENSO forcing to the advective resonance mechanism, we have recontructed the (k, ω) forcing spectrum of SAM and ENSO, from the heat flux patterns shown in Figure 3-9. To do so, we have written the forcing spectrum as a product $E_F(\omega, k) = E_F(\omega)E_F(k)$, in which $E_F(k)$ is simply obtained from a Fourier transform of the (streamline averaged) pattern shown in Figure 3-9c,f, and in which $E_F(\omega)$ is taken as a white noise (with amplitude determined from a linear regression). The latter procedure is justified from a study of the time series associated with the patterns in Figure 3-9c,f which have a decorrelation timescale of about a month (not shown).

The resulting spectra are presented in Figure 3-11. In both spectra, most of the

variability occurs at low wavenumbers; this reflects the spatial pattern of the total heat fluxes, for which $k = 1, 2$ are the dominant Fourier components. Both ENSO and SAM spectra show enhanced power at a timescale of about 10 yr for $k = 1$ and 5yr for $k = 2$ (note that the spectra are continuous in ω but discrete in k), both being in agreement with (3.7). It appears that SAM and ENSO contribute equally to the SST variability.

The short dataset does not warrant a direct comparison with observed spectra but the results obtained in Figure 3-11 are in qualitative agreement with the spatio-temporal characteristics of SST discussed in Section 3.2.3. Decadal variability at low wavenumbers also appears to characterize the SST simulated with ENSO and SAM heat fluxes (Figure 3-10). In particular, a $k = 1$ feature is evident.

3.6 Ocean-atmosphere coupling

In agreement with the modeling results of Weisse et al. [1999] and Haarsma et al. [2000], the present analysis suggests that low-frequency SST variability in the ACC can arise from the resonant response of the ocean to stochastic atmospheric forcing. Such a mechanism does not require ocean-atmosphere coupled dynamics. The identification of ENSO and SAM as drivers of anomalous low-level circulation further supports this hypothesis; SAM exists independently of ocean-atmosphere coupling, and the ENSO signal in the Southern Ocean is not affected by local ocean dynamics.

Since ENSO and SAM are the main generators of temperature anomalies along the path of the ACC (Section 3.4), we suggest that SST variability in the Southern Ocean results primarily from a passive response of the oceanic mixed layer to atmospheric forcing, ocean-atmosphere coupling playing a second-order role.

3.7 Summary and conclusions

The spatial and temporal distribution of SST anomalies in the ACC is studied using observations and conceptual models. Low-frequency variability in the ocean is related to fixed patterns of variability in SLP and anomalous surface forcing: turbulent heat fluxes (Fs) and Ekman advection (Fek).

In summary, our main results are:

(i) A simple model of SST including mean advection and driven by observed anomalous surface forcing (Fs + Fek) provides a zero order picture for SST anomalies along the ACC;

(ii) SAM and ENSO have a strong signature in Fs and Fek over the eastern Pacific, and act as generators of SST anomalies in that sector. The SST anomalies are subsequently advected by the mean current;

(iii) The damping of anomalies is large enough that they can be followed for only a couple of years. We found no indication of global propagation along the ACC.

The mechanisms investigated do not rely on ocean-atmosphere coupling. The generation, propagation and damping of SST anomalies can be understood as a passive response of the ocean mixed layer to stochastic atmospheric forcing. Coupled ocean-atmosphere models might shed further light on the role of air-sea interactions in Southern Hemisphere climate variability, although our results suggest that the teleconnection with ENSO and the subtle asymmetry in the surface pattern of SAM need to be reproduced accurately in order to simulate the surface heat fluxes in the Pacific basin.

Examination of the heat fluxes along the ACC reveals that the air-sea interaction occurs mainly in the Pacific sector. In this region we also observe mode water formation. Subantarctic Mode Water (SAMW) results from deepening of the mixed layer in the winter; in the Southeast Pacific it is exported as Antarctic Intermediate Water

[Sloyan and Rintoul, 2001] and plays an important role in the meridional overturning circulation. Rintoul and England [2002] have argued that SAMW variability in driven principally by Ekman transport, as opposed to local air-sea fluxes. The present study suggests that both mechanisms are important sources of oceanic variability.

Temperature variability also has implications for the interannual variability of CO_2 fluxes in the Southern Ocean. Heat fluxes affect the air-sea exchanges of gas by changing their solubility in seawater; because of its reaction with seawater, oceanic CO_2 equilibrates slowly with atmospheric concentrations. Decadal variability in CO_2 fluxes is detected in data from the high resolution global model of biogeochemical cycles of McKinley et al. [2003] ; it is likely that it arises from stochastic heat fluxes, as in the case of SST. This could be investigated using the framework proposed in this study.

Bibliography

Abraham, E. (1998). The generation of plankton patchiness by turbulent stirring, *Nature* **391**: 577–580.

Alexander, M., Blade, I., Newman, M., Lanzante, J., Lau, N. & Scott, J. (2002). The atmospheric bridge: The influence of ENSO teleconnections on air-sea interaction over the global oceans, *J. Climate* **15**: 2205–2231.

Ashjian, C., Rosenwaks, G., Wiebe, P., Davis, C., Gallager, S., Copley, N., Lawson, G. & Alatalo, P. (2004). Distribution of zooplankton on the continental shelf off Marguerite Bay, Antarctic Peninsula, during austral fall and winter 2001, *Deep-Sea Res. II* **51**: 2073–2098.

Boukal, D. & Berec, L. (2002). Single-species models of the allee effect: extinction boundaries, sex ratios and mate encounters, *J. Theor. Biol.* **218**: 375–394.

Bretherton, C., Smith, C. & Wallace, J. (1992). An intercomparison of methods for finding coupled patterns in climate data, *J. Climate* **5**: 541–560.

Cai, W. & Baines, P. (2001). Forcing of the Antarctic circumpolar wave by El Niño-Southern Oscillation teleconnections, *J. Geophys. Res* **106**(C5): 9019–9038.

Cane, M., Zebiak, S. & Dolan, S. (1986). Experimental forecasts of El-Niño, *Nature* **321**: 827–832.

Czaja, A., van der Vaart, P. & Marshall, J. (2002). A diagnostic study of the role of remote forcing in tropical Atlantic variability, *J. Climate* **15**: 3280–3290.

DeRobertis, A. (2002). Small-scale spatial distribution of the euphausiid *euphausia pacifica* and overlap with planktivorous fishes, *J. Plankton Res* **11**: 1207–1220.

Epstein, A. & Beardsley, R. (2001). Flow-induced aggregation of plankton at a front: a 2-d eulerian model study, *Deep-Sea Res. II* **48**: 395–418.

Flierl, G., Grünbaum, D., Levin, S. & Olson, D. (1999). From individuals to aggregations: the interplay between behavior and physics, *J. Theor. Biol.* **196**: 397–454.

Flierl, G. & McGillicuddy, D. (2002). Mesoscale and submesoscale physical-biological interactions, *The Sea* **12**: 113–185.

Frankignoul, C. (1985). Sea surface temperature anomalies, planetary waves, and air-sea feedback in the middle latitudes, *Review of Geophysics* **23**: 357–390.

Franks, P. (1992). Sink or swim - accumulation of biomass at fronts, *Mar. Ecol. Prog. Ser.* **82**: 1–12.

Genin, A., Jaffe, J., Reef, R., Richter, C. & Franks, P. (2005). Swimming against the flow: a mechanism of zooplankton aggregation, *Science* **308**: 860–862.

Goodman, J. & Marshall, J. (1999). A model of decadal middle-latitude atmosphere-ocean coupled modes, *J. Climate* **12**: 621–641.

Goodman, J. & Marshall, J. (2003). The role of neutral singular vectors in midlatitude air-sea coupling, *J. Climate* **16**: 88–102.

Haarsma, R., Selten, F. & Opsteegh, J. (2000). On the mechanisms of the Antarctic circumpolar wave, *J. Climate* **13**: 1461–1480.

Hall, A. & Visbeck, M. (2002). Synchronous variability in the Southern Hemisphere atmosphere, sea ice, and ocean resulting from the annular mode, *J. Climate* **15**: 3043–3057.

Hamilton, W. (1971). Geometry for the selfish herd, *J. Theor. Biol.* **31**: 295–311.

Hasselmann, K. (1976). Stochastic climate models. Part 1. Theory, *Tellus* **28**: 473–485.

Kalnay, E. & Coauthors (1996). The NCEP/NCAR 40-year reanalysis project, *Bull. Amer. Meteor. Soc* **77**: 437–471.

Karoly, D. (1989). Southern Hemisphere circulation features associated with ENSO events, *J. Climate* **2**: 1239–1252.

Karsten, R. & Marshall, J. (2002). Constructing the residual circulation of the ACC from observations, *J. Phys. Oceanogr* **32**: 3315–3327.

Kushnir, Y., Seager, R. & Miller, J. (2002). A simple coupled model of tropical Atlantic decadal climate variability, *Geophys. Res. Lett* **29**: 48.1–4.

Latif, M. & Barnett, T. (1994). Causes of decadal climate variability over the North Pacific and North America, *Science* **266**: 634–637.

Levin, S. (1994). Patchiness in marine and terrestrial systems: from individuals to populations, *Phil. Trans. Royal Soc. Lond. B* **343**: 99–103.

Levitus, S. & Boyer, T. (1994). *World Ocean Atlas 1994*, Vol. 4, NOAA Atlas NEDSIS 4, U.S. Department of Commerce, Washington D.C.

Lévy, M. & Klein, P. (2004). Does the low frequency variability of mesoscale dynamics explain a part of the phytoplankton and zooplankton spectral variability?, *Proc. Royal Soc. Lond.* **460**: 1673–1683.

Liu, J., Yuan, X., Rind, D. & Martinson, D. (2002). Mechanism study of the ENSO and southern high latitude climate teleconnections, *Geophys. Res. Lett* **29**: 1679.

Mackas, D. & Boyd, C. (1979). Spectral analysis of zooplankton spatial heterogeneity, *Science* **204**: 62–64.

Marr, J. (1962). The natural history and geography of the antarctic krill (*euphausia superba*), *Discovery Rep* **32**: 33–464.

Marshall, J. & Coauthors (2001). North Atlantic climate variability: Phenomena, impacts and mechanisms, *International Journal of Climatology* **21**: 1863–1898.

McKinley, G., Follows, M. & Marshall, J. (2003). Interannual variability of air-sea O_2 fluxes and the determination of CO_2 sinks using atmospheric O_2/N_2, *Geophys. Res. Lett* **30**: 1101.

Miller, D. & Hampton, I. (1989). *Biology and ecology of the Antarctic krill (Euphausia superba Dana): A review*, BIOMASS Sci. Ser. No. 9.

Nakamura, H. & Shimpo, A. (2004). Seasonal variations in the Southern Hemisphere storm tracks and jet streams as revealed in a reanalysis dataset, *J. Climate* **17**: 1828–1844.

Okubo, A. (1980). *Diffusion and Ecological Problems: Mathematical Models*, Biomathematics, Vol 10, Heidelberg: Springer-Verlag, 254 pp.

Okubo, A. (1986). Dynamical aspects of animal grouping: swarms, schools, flocks, and herds, *Adv. Biophys.* **22**: 1–94.

Parrish, J. & Edelstein-Keshet, L. (1999). Complexity, pattern, and evolutionary trade-offs in animal aggregation, *Science* **284**: 99–101.

Pascual, M., Mazzega, P. & Levin, S. (2001). Oscillatory dynamics and spatial scale: the role of noise and unresolved pattern, *Ecology* **82**: 2357–2369.

Pasquero, C. (2005). Differential eddy diffusion of biogeochemical tracers, *Geophys. Res. Lett.* **32**: L17603, doi:10.1029/2005GL023662.

Pierrehumbert, R. (2000). Lattice models of advection-diffusion, *Chaos* **10**: 61–74.

Qiu, B. & Jin, F.-F. (1997). Antarctic circumpolar waves: an indication of ocean-atmosphere coupling in the extratropics, *Geophys. Res. Lett* **24**: 2585–2588.

Rintoul, S. & England, M. (2002). Ekman transport dominates local air-sea fluxes in driving variability of subantarctic mode water, *J. Phys. Oceanogr* **32**: 1308–1321.

Saravanan, R. & McWilliams, J. (1998). Advective ocean-atmosphere interaction: An analytical stochastic model with implication for decadal variability, *J. Climate* **11**: 165–188.

Scott, R. (2003). Predictability of SST in an idealized, one-dimensional, coupled atmosphere-ocean climate model with stochastic forcing and advection, *J. Climate* **16**: 323–335.

Sloyan, B. & Rintoul, S. (2001). Circulation, renewal, and modification of Antarctic mode and intermediate water, *J. Phys. Oceanogr* **31**: 1005–1030.

Sterl, A. (2004). On the (in)homogeneity of reanalysis products, *J. Climate* **17**: 3866–3873.

Talley, L. (1999). Simple coupled midlatitude climate models, *J. Phys. Oceanogr* **29**: 2016–2037.

Thompson, D. & Wallace, J. (2000). Annular modes in the extratropical circulation. Part I: Month-to-month variability, *J. Climate* **13**: 1000–1016.

Ward, P. (2005). WWW page, http://www.coolantarctica.com/antarctica fact file /wildlife/whales/food web.htm.

Weber, L., El-Sayed, S. & Hampton, I. (1986). The variance spectra of phytoplankton, krill and water temperature in the antarctic ocean south of africa, *Deep-Sea Res.* **33**: 1327–1343.

Weisse, R., Mikolajewicz, U., Sterl, A. & Drijfhout, S. (1999). Stochastically forced variability in the Antarctic circumpolar current, *J. Geophys. Res* **104**(C5): 11049–11064.

White, W., Chen, S.-C. & Peterson, R. (1998). The Antarctic circumpolar wave: A beta effect in ocean-atmosphere coupling over the Southern Ocean, *J. Phys. Oceanogr* **28**: 2345–2361.

White, W. & Peterson, R. (1996). An Antarctic circumpolar wave in surface pressure, wind, temperature and sea ice extent, *Nature* **380**: 699–702.

Whitworth, T. (1988). The Antarctic circumpolar current, *Oceanus* **31**: 53–58.

Wunsch, C. (1999). The interpretation of short climate records, with comments on the North Atlantic and southern oscillations, *Bull. Am. Met. Soc* **80**: 245–255.

Yuan, X. & Martinson, D. (2000). Antarctic sea ice extent variability and its global connectivity, *J. Climate* **13**: 1697–1717.

Zhou, M. & Dorland, R. (2004). Aggregation and vertical migration behavior of *euphausia superba*, *Deep-Sea Res. II* **51**: 2119–2137.

Zhou, M. & Huntley, M. (1996). The principle of biological attraction, demonstrated by the bio-continuum theory of zooplankton patch dynamics, *J. Mar. Res.* **54**: 1017–1037.